Earth-Science Reviews xxx (xxxx) xxx–xxx

Contents lists available at ScienceDirect

Earth-Science Reviews

journal homepage: www.elsevier.com/locate/earscirev

Cooling-driven oceanic anoxia across the Smithian/Spathian boundary (mid-Early Triassic)

Huyue Song[a,*], Yong Du[a], Thomas J. Algeo[a,b,c], Jinnan Tong[a], Jeremy D. Owens[d], Haijun Song[a], Li Tian[a], Haiou Qiu[e], Yuanyuan Zhu[f], Timothy W. Lyons[g]

[a] State Key Laboratory of Biogeology and Environmental Geology, School of Earth Sciences, China University of Geosciences, Wuhan 430074, China
[b] State Key Laboratory of Geological Processes and Mineral Resources, China University of Geosciences, Wuhan 430074, China
[c] Department of Geology, University of Cincinnati, Cincinnati, OH 45221-0013, USA
[d] Department of Earth, Ocean, and Atmospheric Science, Florida State University, Tallahassee, FL 32306-4520, USA
[e] Faculty of Material Science and Chemistry, China University of Geosciences, Wuhan 430074, China
[f] Wuhan Institute of Geology and Mineral Resources, Wuhan 430205, China
[g] Department of Earth Sciences, University of California, Riverside, CA 92521, USA

ARTICLE INFO

Keywords:
Organic carbon burial
Carbon isotopes
Sulfur isotopes
Primary productivity
South China

ABSTRACT

The Smithian/Spathian boundary (SSB) represents a major climatic-oceanic-biotic event within the ~5-Myr-long recovery interval of the Early Triassic following the end-Permian mass extinction. The SSB was associated with pronounced cooling following the middle Smithian hyper-greenhouse, a ~ +2 to +8‰ positive carbon isotope excursion, and a second-order mass extinction, yet its underlying cause(s) remain poorly understood. Here, we review oceanic environmental changes during the middle Smithian to early Spathian interval and their potential mechanisms. In addition, we undertook an analysis of the carbon-sulfur-iron (C-S-Fe) systematics of the South Majiashan section, which was located on the paleo-western margin of the South China Craton during the Early Triassic, to better understand the causation of these environmental changes. This analysis revealed low $\delta^{13}C_{carb}$ (i.e., the N3 minimum) in the middle Smithian but rapidly rising $\delta^{13}C_{carb}$ (i.e., to the P3 maximum) and $\delta^{34}S_{CAS}$ within the SSB interval (i.e., late Smithian-earliest Spathian). Both the middle Smithian and SSB intervals are marked by development of marine euxinia, which we hypothesize had fundamentally different causes. The middle Smithian was associated with hyperwarming (the "Smithian Thermal Maximum"), which was probably triggered by a peak in magmatic activity of the Siberian Traps LIP. In contrast, the SSB interval was associated with global climatic cooling, which may have stimulated oceanic overturning circulation and upwelling on continental margins, leading to transient local increases in marine productivity and expansion of oceanic oxygen-minimum zones (OMZs). The concurrent positive excursions in $\delta^{13}C_{carb}$ and $\delta^{34}S_{CAS}$ at South Majiashan and other sections worldwide are evidence of enhanced burial of organic carbon and pyrite on a regional or global scale, as well as of a concurrent decline in atmospheric pCO_2 that may have positively re-enforced the SSB cooling event.

1. Introduction

The end-Permian mass extinction at ~252-Ma was the largest biotic crisis of the Phanerozoic (Raup and Sepkoski Jr., 1982; Sepkoski Jr., 1986; Erwin, 1993; Bottjer et al., 2008; Song et al., 2013a; Stanley, 2016). The ensuing ~5-Myr-long Early Triassic was a highly unsettled interval (Bottjer et al., 2008; Chen and Benton, 2012), as shown by large-scale flood basalt magmatism (Sobolev et al., 2011), multiple perturbations to the marine carbon and sulfur cycles (e.g. Payne et al., 2004; Algeo et al., 2008; Marenco et al., 2008; Luo et al., 2010; Song et al., 2013b; Song et al., 2014a), widespread ocean anoxia/euxinia (e.g., Lau et al., 2016; Elrick et al., 2017; Zhang et al., 2018a,Zhang et al., 2018b), and strong climate warming (Joachimski et al., 2012; Sun et al., 2012; Romano et al., 2013). The acme of this disturbed interval came during the middle Smithian (e.g., *Flemingites rursiradiatus* beds and *koeneni* beds in South China; see Galfetti et al., 2007a) of the Early Triassic (~1.0–1.5 Myr after the end-Permian crisis), when tropical seawater temperatures may have reached 38–40 °C (Sun et al., 2012) and marine carbonate $\delta^{13}C$ reached highly negative values (e.g., Payne et al., 2004; Galfetti et al., 2007b; Tong et al., 2007) (Fig. 1).

* Corresponding author.
E-mail address: hysong@cug.edu.cn (H. Song).

https://doi.org/10.1016/j.earscirev.2019.01.009
Received 13 October 2018; Received in revised form 10 January 2019; Accepted 11 January 2019

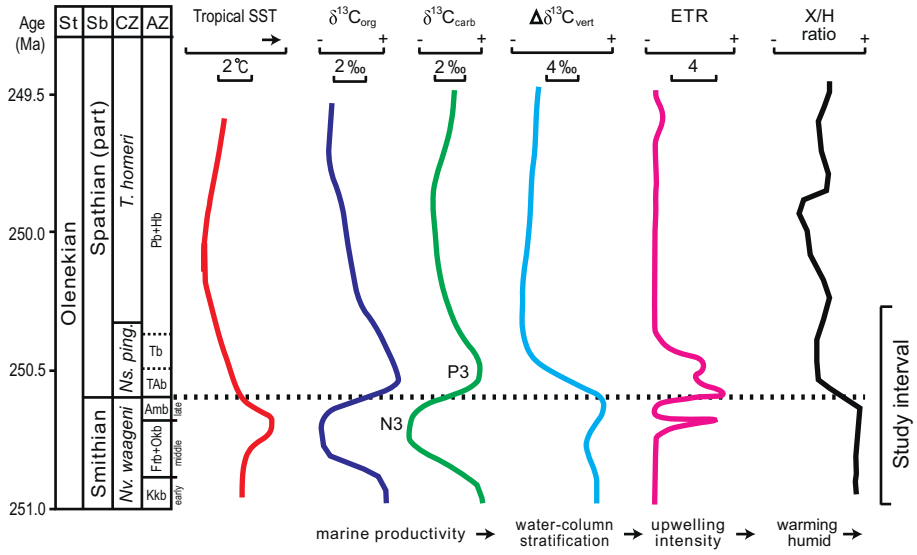

Fig. 1. General trends in marine environmental conditions from the middle Smithian to early Spathian. Higher marine productivity, more intense water-column stratification, and increased upwelling intensity are indicated by arrows. The parallel paleotemperature curves are derived from surface-water (*Pachycladina* and *Platyvillosus*) versus deeper conodont taxa (*Neospathodus*). Sources: paleotemperatures (Sun et al., 2012, modified after corrections of Goudemand, 2014 and Zhang et al., 2019), carbon isotopes (Galfetti et al., 2007b; Tong et al., 2007), vertical $\delta^{13}C_{DIC}$ gradient (Song et al., 2013a), ETR (Saito et al., 2013) and X/H ratio (Galfetti et al., 2007b). The age scale and N3 and P3 carbon-isotope excursions are from Song et al. (2013b). Abbreviations: ETR = extended tricyclic terpane ratio, X/H = xerophytic/hygrophytic, SST = sea-surface temperature, St = stage, Sb = substage, CZ = simplified conodont subdivisions, AZ = simplified Chinese ammonoid subdivisions (see Galfetti et al., 2007a; note that these ammonoid zones are actually not continuous); *Nv.* = *Novispathodus*, *Ns.* = *Neospathodus*, *T.* = *Triassospathodus*, *ping.* = *pingdingshanensis*, Kkb = *Kashmirites kapila* beds, Frb = *Flemingites rursiradiatus* beds, Okb = *Owenites koeneni* beds, Amb = *Anasibirites multiformis* beds, TAb = Tirolitid n. gen. A beds, Tb = *Tirolites* beds, Pb = *Procolumbites* beds, Hb = *Hellenites* beds. The stratigraphic interval of the South Majiashan study section is shown at right.

Following the extreme conditions of the Smithian Substage, the Spathian Substage was characterized by ameliorated climatic and oceanic environmental conditions (Algeo et al., 2011a) and a potentially more sustained marine faunal recovery (Bottjer et al., 2008; Song et al., 2011; Chen and Benton, 2012). However, the ~120- to 200-kyr-long transition from the late Smithian to the early Spathian (see Brühwiler et al., 2010, for estimates of ammonoid zone duration) was characterized by rapid changes in the marine carbon and sulfur cycles, an oceanic anoxic event, and strong climatic cooling (e.g. Zhang et al., 2015; Stebbins et al., 2018a, 2018b). Proxy records reveal large positive excursions (up to 6‰) of both $\delta^{13}C_{carb}$ and $\delta^{13}C_{org}$ (Payne et al., 2004; Tong et al., 2007; Galfetti et al., 2007b; Grasby et al., 2013), a sharp reduction in the vertical $\delta^{13}C$ gradient of oceanic dissolved inorganic carbon ($\Delta\delta^{13}C_{vert}$, means the difference of the $\delta^{13}C$ between the shallow and deep water) (Song et al., 2013a), a cooling of tropical sea-surface temperatures (SST) based on conodont oxygen isotopes (Sun et al., 2012; Romano et al., 2013), and an increase in upwelling intensities based on extended tricyclic terpane ratios (ETR) at Chaohu section from South China (Saito et al., 2013; Fig. 1). The Smithian-early Spathian also witnessed changes in land plant assemblages, with a spore peak in the mid-Smithian yielding to a recovery of gymnosperms during the late Smithian and early Spathian (Hermann et al., 2011, 2012). The late Smithian also corresponds to a major second-order mass extinction for at least nekto-pelagic organisms such as ammonoid and conodonts (e.g., Orchard, 2007; Jattiot et al., 2016). Additionally, ammonoid assemblages exhibit distinct changes, with cosmopolitan faunas of the late Smithian reflecting a low equator-to-pole sea-surface temperature (SST) gradient, and development of greater latitudinal diversity in the early Spathian due to a steepening of the SST gradient (Brayard et al., 2006, 2009).

The causes of these far-reaching changes in marine systems during the Smithian-Spathian transition have not been determined to date. In this study, we first review carbon-isotope, temperature, and redox records for the middle Smithian to early Spathian. We then analyze an important Olenekian succession, the South Majiashan section (31°37′17.77″N, 117°49′9.64″E) of the Chaohu area of Anhui Province in eastern China, which is a candidate for the Induan-Olenekian boundary global stratotype section and point (GSSP) (Tong et al., 2004a). We generated multiple geochemical proxies, including carbon and sulfur isotopes, iron speciation, and pyrite framboid size distributions, for the South Majiashan section and then compared our results with equivalent data for other SSB sections from South China, Canada, western USA, and India (Song et al., 2014a; Zhang et al., 2015; Thomazo et al., 2018; Stebbins et al., 2018a, 2018b). Our goals in this investigation were (1) to better understand changes in marine redox conditions, the global carbon and sulfur cycles, and general oceanographic conditions at the SSB interval, and (2) to draw inferences concerning their underlying causes and their relationship to contemporaneous biotic changes.

2. Early Triassic global background

The sequence of events during the SSB interval and their interrelationships have not been correctly delineated in some earlier studies, owing to the shortness of the transition interval (~120 to 200 kyr), the low temporal resolution of some studies, and inconsistencies in placement of the SSB (see Zhang et al., 2019, for a review). Although oceanic anoxia was widespread during the Smithian to early Spathian (Section 2.3), but this does not mean that oceanic environmental conditions and watermass dynamics were unchanged during this interval. We emphasize that it is important to distinguish middle Smithian events from SSB events, because these two intervals exhibited distinct differences in (1) carbon cycling, with the middle Smithian characterized by a $\delta^{13}C$ minimum (N3) and the SSB interval by a shift toward a $\delta^{13}C$ maximum (P3) (Section 2.1), and (2) tropical SSTs, with the middle Smithian marked by hyperwarming ("Smithian Thermal Maximum"; Zhang et al., 2019) and the SSB interval by rapid cooling (Section 2.2).

2.1. Carbon-cycle perturbations

The Early Triassic witnessed some of the largest carbon-isotopic excursions of the Phanerozoic (Payne et al., 2004; Tong et al., 2007; Horacek et al., 2007, 2009; Song et al., 2013a; Song et al., 2014a; Song et al., 2018). Early Triassic $\delta^{13}C_{carb}$ profiles show negative excursions during the latest Changhsingian to earliest Griesbachian, early Dienerian, early to late Smithian, and middle Spathian (N1 to N4, respectively; standard numbering system of Song et al., 2013b, Song et al., 2014a), with similar patterns in $\delta^{13}C_{org}$ records (Grasby et al., 2013; Meyer et al., 2013; Romano et al., 2013; Caravaca et al., 2017). Various hypotheses have been proposed to account for these negative excursions, including influx of isotopically light carbon from massive volcanism or methane oxidation (Berner, 2002; Payne and Kump, 2007;

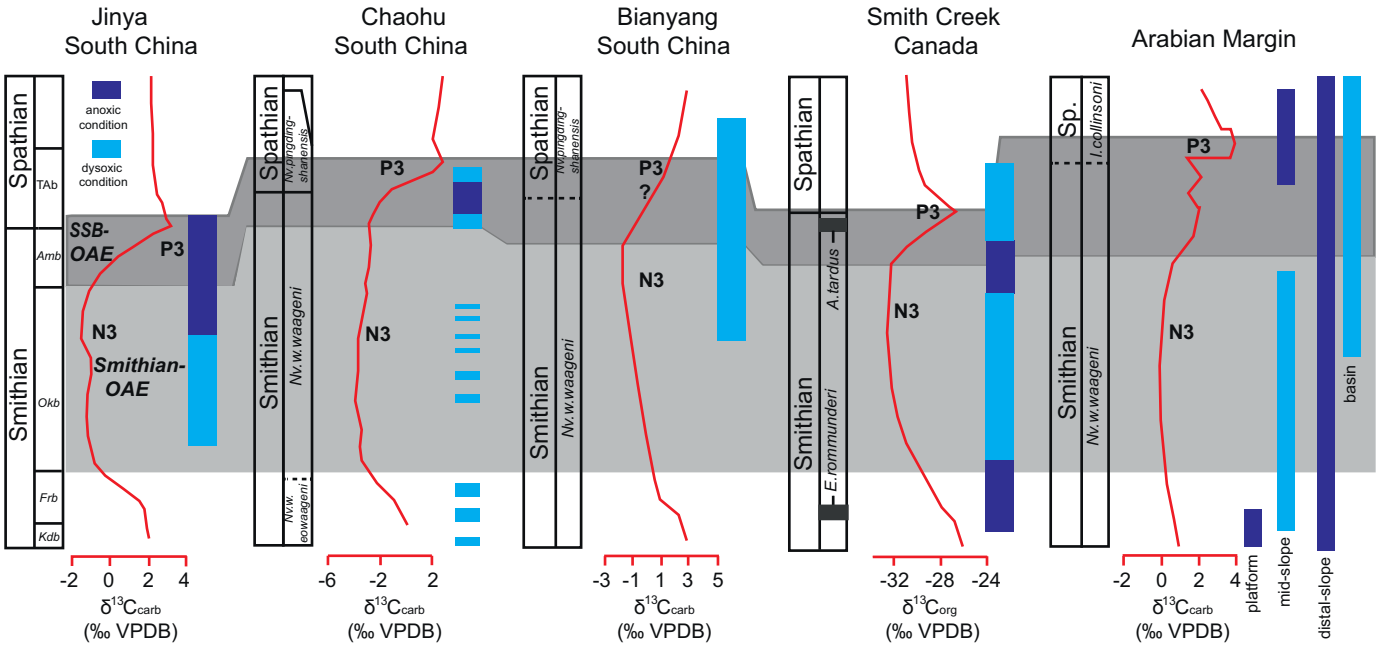

Fig. 2. The middle Smithian ocean anoxic event (Smithian-OAE) and Smithian-Spathian boundary ocean anoxic event (SSB-OAE). Data sources: Jinya (Galfetti et al., 2007a); Chaohu (Huang et al., 2017); Bianyang (Tian et al., 2014); Smith Creek (Grasby et al., 2013); Arabian Margin (Clarkson et al., 2016). Sp. = Spathian; A. = *Anawasatchites*; E. = *Euflemingites*; I. = *Icriospathodus* and see Fig. 1 for other abbreviations.

Shen et al., 2012; Burgess et al., 2017), mixing of the stratified oceanic watermasses (Horacek et al., 2007, 2009), soil erosion (Sephton et al., 2005; Algeo and Twitchett, 2010), and decreased marine productivity (Algeo et al., 2011b, 2013; Song-HY et al., 2013). In addition, a local diagenetic influence on the Smithian-Spathian $\delta^{13}C$ excursion of the Thaynes Group in Utah has been proposed (Thomazo et al., 2016).

The intervals between these negative carbon-isotopic excursions are marked by positive excursions (or a rebound from negative values to more typical marine $\delta^{13}C$ values; Payne et al., 2004; Tong et al., 2007; Song et al., 2013a, Song et al., 2014a). The SSB, in particular, is characterized by a large positive shift, from −2/−5‰ (N3) to +4/+6‰ (P3), with the SSB coinciding with approximately the mid-point of the isotopic shift (Fig. 1) (Zhang-L et al., 2019). Large positive excursions (up to 8‰) of both $\delta^{13}C_{carb}$ and $\delta^{13}C_{org}$ are observed at the SSB in nearly all sections globally, including in all major Triassic ocean basins (Fig. 2 and S1) (Payne et al., 2004; Tong et al., 2007; Galfetti et al., 2007b; Horacek et al., 2007, 2009; Brühwiler et al., 2009; Grasby et al., 2013; Wignall et al., 2016; Caravaca et al., 2017). These positive excursions are generally explained as the result of increased primary productivity and organic carbon burial during the SSB interval.

2.2. Sea-surface temperatures

Temperature changes (warming or cooling) have long been speculated on as a factor in the Permian-Triassic boundary (PTB) mass extinction (Yin et al., 1992; Erwin, 1993). A negative $\delta^{18}O$ shift in whole-rock carbonates from the Carnic Alps of Austria suggested climatic warming of ~5–6 °C around the PTB, although possible influences from salinity and/or diagenesis could not be excluded (Holser et al., 1989). Later researchers inferred warming during the PTB based on co-occurrence with Siberian Traps volcanism and likely increases in atmospheric CO_2 emissions (Renne et al., 1995; Svensen et al., 2009; Korte et al., 2010). Joachimski et al. (2012) presented the first high-resolution conodont apatite $\delta^{18}O$ temperature curve for the PTB, demonstrating a 2‰ decrease (equivalent to ~8 °C warming) immediately before the main extinction phase. This finding was supported by O-isotope studies of exceptionally preserved brachiopods (Brand et al., 2012) and micritic limestones (Schobben et al., 2014) in PTB sections. The PTB temperature increase coincided with a large negative $\delta^{13}C$ excursion, implying that climatic warming was due to inputs of isotopically light greenhouse gases, possibly from the Siberian Traps Large Igneous Province (Korte et al., 2010). However, a recent study using laser-ablation conodont apatite $\delta^{18}O$ inferred that the rapid PTB warming followed the initial negative $\delta^{13}C$ shift and the onset of the mass extinction, implying that climate warming was not the prime cause of the biocrisis (Chen et al., 2016).

Conodont apatite $\delta^{18}O$ studies have also shed light on long-term paleo-temperature change through the Early Triassic (Sun et al., 2012; Romano et al., 2013). These studies from tropical oceans showed that hyperthermal conditions (SST > 35 °C) existed during the latest Changhsingian to early Dienerian, middle Smithian (i.e., the "Smithian Thermal Maximum"; Zhang et al., 2019), and middle to late Spathian, with relatively cooler (but still warm) conditions during the mid-Dienerian to early Smithian, latest Smithian to early Spathian, and latest Spathian.

The SSB interval coincided with the strongest cooling event of the Early Triassic, marked by a rapid mean temperature decrease of at least 4 °C (Sun et al., 2012; Romano et al., 2013). Although tropical sea-surface temperatures remained warm (~32 °C) during the early Spathian, the SSB thus coincided with a significant climate amelioration that followed closely upon the Smithian hyperwarming event. Cooling during the SSB interval coincided with the replacement of endemic taxa with more cosmopolitan taxa among ammonoid faunas (Brayard et al., 2006, 2007, 2009; Jattiot et al., 2016, 2018). Because it coincided with positive excursions of both $\delta^{13}C_{carb}$ and $\delta^{13}C_{org}$ globally, this cooling event was presumably triggered by drawdown of atmospheric pCO_2 in response to a massive increase in organic carbon burial during the SSB interval (Galfetti et al., 2007b).

2.3. Ocean-redox conditions

Widespread oceanic anoxia is thought to have been a key factor in the PTB biocrisis (Isozaki, 1997; Algeo et al., 2011a). Redox conditions at the PTB have long received attention (e.g., Wignall and Twitchett, 1996; Grice et al., 2005; Algeo et al., 2008; Song et al., 2014b; Shen et al., 2016), but recent work has provided new insights into redox

variation during the Early Triassic at both global and regional scales. Carbonate U-isotope studies provide records of changes in average global-ocean conditions, with several peaks during the Early Triassic (Lau et al., 2016; Elrick et al., 2017) including one at the SSB (Zhang et al., 2018a,Zhang et al., 2018b). Based on trace-metal concentrations, iron species, pyrite framboid sizes, and lithologies (e.g., black shale), the SSB interval is inferred to have coincided with expanded oceanic anoxia in the eastern Paleo-Tethys (Galfetti et al., 2007a, 2008; Song et al., 2012; Tian et al., 2014; Wei et al., 2015; Huang et al., 2017, Fig. S1), northwestern Pangea (Grasby et al., 2013), and southern Neo-Tethys (Clarkson et al., 2016). Parallel positive excursions of carbon and sulfur isotopes at Jesmond (western Canada) and Spiti Valley (India) imply enhanced organic carbon and pyrite burial at a global scale during the SSB interval (Stebbins et al., 2018a, 2018b). However, some studies have inferred oxic/suboxic conditions during the SSB interval based on elemental data and lithologies, e.g., at Tulong in South Tibet and at Shitouzhai in South China (Brühwiler et al., 2009; Zhang et al., 2015).

The available evidences suggest that Early Triassic oceans were characterized by strongly fluctuating but episodically intense anoxia. Although ocean-redox conditions were spatially variable, they exhibited a strong depth-dependency, with the most intensely reducing conditions located in the oceanic thermocline region (Algeo et al., 2011b; Winguth and Winguth, 2012). Intensified anoxia within the thermocline is expressed on some continental margins in the development of anoxic facies on the distal outer shelf/upper slope (e.g., Arabian Margin; Clarkson et al., 2016). The depth dependency of ocean-redox conditions during the Early Triassic was due to some potential combination of enhanced oceanic stratification (Song et al., 2013a) and increased primary productivity (Meyer et al., 2011; Algeo et al., 2013; Shen et al., 2015).

For most of the Early Triassic, oceanic anoxic events were associated with negative $\delta^{13}C$ excursions and climatic warming (Song et al., 2014a; Zhang et al., 2018b). Such intervals (e.g., the middle Smithian) were also characterized by high terrestrial weathering rates, which is consistent with both peak warming (an enhancer of weathering) and oceanic anoxia (a response to higher riverine nutrient fluxes) (Wei et al., 2015). This pattern suggests a relationship to intervals of large-scale activity of the Siberian Traps (Song et al., 2014a). In contrast, the existing evidence indicates that anoxia during the SSB interval was associated with a positive $\delta^{13}C$ shift and climatic cooling (Sun et al., 2012). This implies that a different, as-yet poorly understood mechanism was responsible for the development of marine anoxia during the Smithian-Spathian boundary event.

3. Case study of south Majiashan section

3.1. Geologic background

During the Early Triassic, the shallow Yangtze carbonate platform occupied the central part of the South China Craton (Fig. 3). This platform was bounded to the west by a ramp descending to a deepwater basin that bordered the Qinling Ocean, which was the easternmost extension of the Paleo-Tethys Ocean (note: all directional references for the South China Craton are prior to a ~80–90° post-Triassic clockwise rotation of the craton). The South Majiashan study section was deposited at the distal end of this ramp at estimated water depths of 300–500 m (Feng et al., 1997; Tong et al., 2004b; Li et al., 2007). The western margin of the South China Craton was an area of locally enhanced upwelling, possibly due to offshore Ekman transport, during the SSB interval (Saito et al., 2013).

The Lower Triassic of the Chaohu area is well exposed in local road and quarry cuts and consists of relatively unweathered limestone and marlstone strata with thin shale interbeds. The lower (Induan) part of the succession is dominated by marlstone and the upper part (of Olenekian age) by limestone. These strata have been assigned (in ascending stratigraphic order) to the Yinkeng, Helongshan, and Nanlinghu formations (Fig. 4). The succession has been well-studied with respect to its conodont, bivalve, and ammonoid biostratigraphy, and it has been correlated in detail with other Lower Triassic sections in South China and globally (Tong et al., 2004b; Zhao et al., 2007). In the nearby West Pingdingshan section, the base of Subbed 24–16 coincided with the first appearance datum (FAD) of the conodont *Neospathodus waageni*, a marker for the base of the Smithian Substage (Zhao et al., 2007). The FAD of the conodont *N. pingdingshanensis*, an informal marker for the SSB, is located ~1.5 m below the Helongshan-Nanlinghu formation contact (Liang et al., 2011).

The stratigraphic range of the 60-m-thick South Majiashan study section is from the early Smithian to the early Spathian (Fig. 4). The uppermost 3.6 m of the Helongshan Formation contains a distinctive dark gray to black marlstone unit (BMU) that represents the only significant concentration of organic matter (TOC > 1%) within the Lower Triassic of the Chaohu area (Fig. 4A). The BMU includes both non-calcareous and calcareous beds, with 12 of 18 study samples yielding < 50% $CaCO_3$ (mean 23 ± 15%) and the remaining samples containing > 50% $CaCO_3$ (Table S1). Biostratigraphic studies have suggested that the SSB is located within the BMU (Tong et al., 2004b; Zhao et al., 2007; Liang et al., 2011), a placement that is supported by the major positive shift in $\delta^{13}C_{carb}$ (Fig. 4B), which is a globally correlatable feature of the SSB (e.g., Tong et al., 2007).

The age range and average sedimentation rates of the study section can be estimated from existing geochronological constraints. The lower 42 m of the study section represents most (~80%) of the Smithian Substage (~0.7 Myr duration; Ovtcharova et al., 2006; Galfetti et al., 2007a; Brühwiler et al., 2010), yielding an average sedimentation rate of ~75 m Myr^{-1}. The BMU may be stratigraphically condensed, as evidenced by rapid, concurrent shifts in $\delta^{13}C_{carb}$ and $\delta^{34}S_{CAS}$ (Fig. 4B, F), suggesting a lower (but indeterminate) sedimentation rate through this interval.

3.2. Methods

3.2.1. Sampling, total organic carbon, and $\delta^{13}C_{carb}$

We collected 18 samples from the 3.6-m-thick BMU at an average sampling interval of ~20 cm. We also collected 27 samples from the remainder of the South Majiashan section at intervals of ~2 m; these carbonate samples include 19 from strata below the BMU and 8 from strata above the BMU (here collectively termed "non-BMU beds"). Samples were prepared for geochemical analysis by trimming away any veins and surficial weathered rinds and grinding to a powder using a tungsten ball mill. Total inorganic (TIC) and organic carbon (TOC) concentrations were measured using an Eltra 2000C—S analyzer at the University of Cincinnati. Organic carbon was determined by acidizing an aliquot of each sample in 1 N HCl for 6 h at 50 °C, followed by rinsing and filtering. Inorganic carbon was determined as the difference between total carbon and organic carbon. Data quality was monitored via repeated analysis of the USGS standard SDO-1 (9.68% total carbon), which yielded an analytical precision (2σ) of ± 2.5% of reported carbon values.

For carbonate carbon isotope analysis, about 150–400 μg of powdered sample was placed in a 10-mL Na-glass vial, sealed with a butyl rubber septum, and reacted with 100% phosphoric acid at 72 °C after flushing with helium. The evolved CO_2 gas was analyzed for $\delta^{13}C$ and $\delta^{18}O$ using a MAT 253 mass spectrometer coupled directly to a Finnigan Gasbench II interface (Thermo Scientific) at the China University of Geosciences-Wuhan (CUG). Isotopic values are reported as per mille relative to the Vienna Pee Dee belemnite (VPDB) standard. Data quality was monitored via repeated analysis of two Chinese national standards, GBW 04416 ($\delta^{13}C$ = +1.61‰, $\delta^{18}O$ = −11.59‰) and GBW 04417 ($\delta^{13}C$ = −6.06‰, $\delta^{18}O$ = −24.12‰), which yielded analytical precisions (2σ) of better than ± 0.1‰ for $\delta^{13}C$ and $\delta^{18}O$.

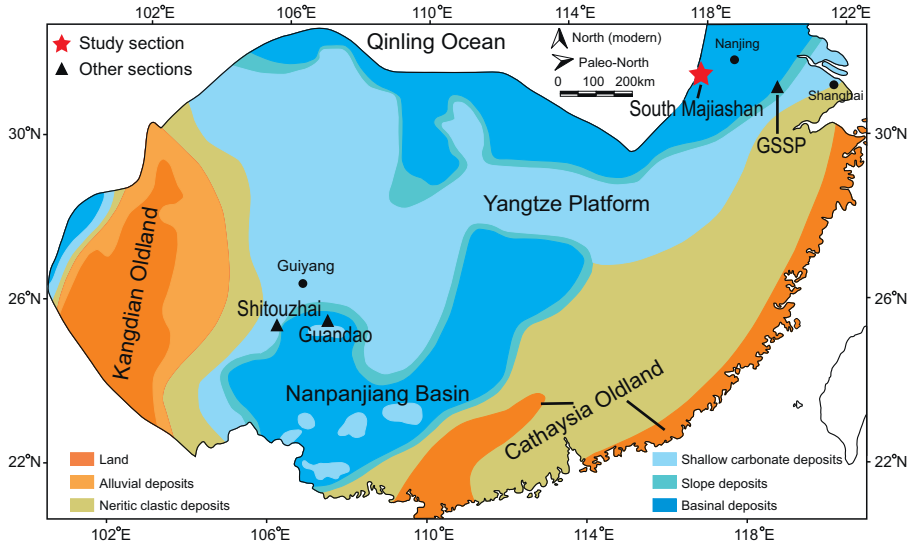

Fig. 3. Early Triassic paleogeography of South China. Modified from Feng et al. (1997). The South Majiashan study section represents a deep ramp setting on the northern margin of the Yangtze Platform downslope from the Meishan GSSP, the Shitouzhai section a shallow carbonate shelf on the southern margin of the Yangtze Platform, and the Guandao section an upper slope setting on the northern margin of the Great Bank of Guizhou (GBG).

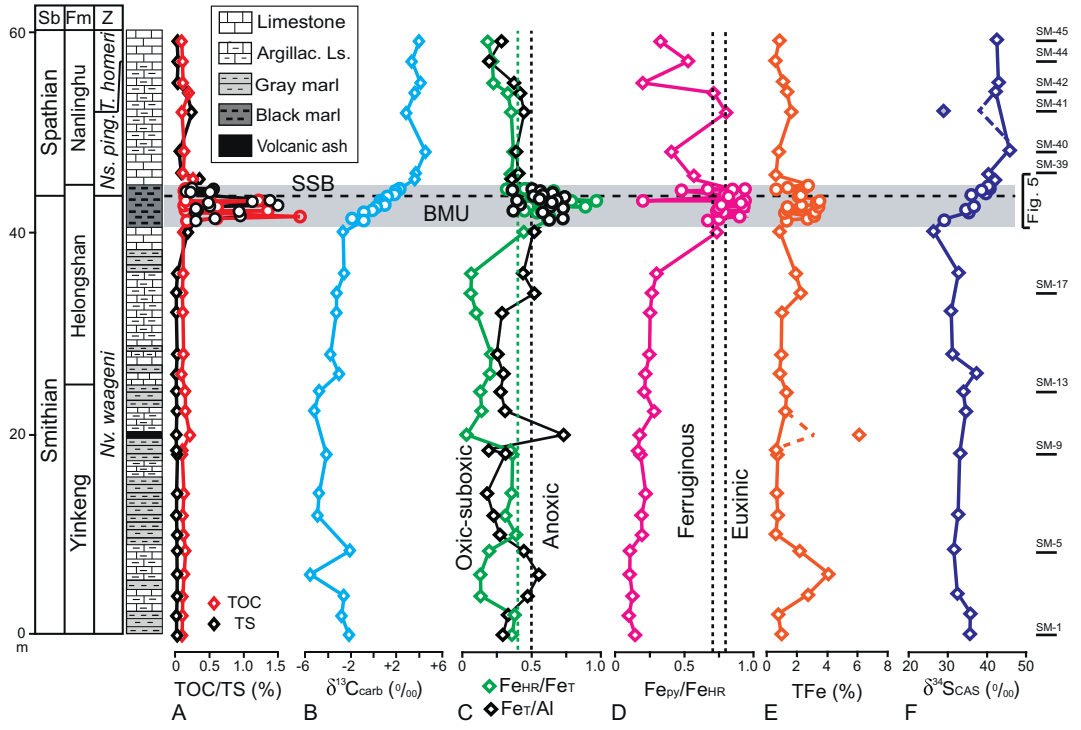

Fig. 4. Chemostratigraphy of the full South Majiashan study section: (A) total organic carbon (TOC), (B) carbonate $\delta^{13}C$, (C) highly reactive Fe:total Fe (Fe_{HR}/Fe_T), (D) pyrite Fe/highly reactive Fe (Fe_{PY}/Fe_{HR}), (E) total Fe (Fe_T), and (F) carbonate-associated sulfate $\delta^{34}S$ ($\delta^{34}S_{CAS}$). The Smithian/Spathian boundary (SSB) is marked by a distinctive black mudstone unit (BMU). On the right are shown the stratigraphic interval of Fig. 5 and the positions of 10 non-BMU samples analyzed for pyrite framboid content (only SM-39 contained framboids). The dashed vertical lines at 0.40 (Fe_{HR}/Fe_T) and 0.70–0.80 (Fe_{py}/Fe_{HR}) represent thresholds for oxic-dysoxic vs. anoxic conditions and ferruginous vs. euxinic conditions, respectively (from Poulton and Canfield, 2011). Conodont biozonation from Zhao et al. (2007) and Liang et al. (2011). Fm = formation; argill. ls. = argillaceous limestone; other abbreviations as in Figs. 1 and 2. The open circles and diamonds represent the samples in the BMU interval and non-BMU interval respectively.

3.2.2. Sulfur isotopes

Carbonate-associated sulfate (CAS) was extracted using the method of Burdett et al. (1989) as modified by Song et al. (2014a). For each sample, about 100–150 g of powder was rinsed in a 10% NaClO solution for 24 h. After gravitational settling, the supernatant was decanted, and the residual powder was rinsed with 18.25-MΩ distilled water. The residual material was then washed for 24 h in a 6% NaClO solution. The supernatant was decanted again, and the residual powder was rinsed in 18.25-MΩ distilled water to dilute and remove any residual NaClO solution. The residual powder was then dissolved in 6-M HCl for 12 h. The mixture was filtered through a 0.45-μm membrane to remove any insoluble material. A 10% $BaCl_2$ solution was added to the filtrate in order to precipitate $BaSO_4$, which was then dried and weighed. The $BaSO_4$ was mixed with V_2O_5 and SiO_2 and combusted under vacuum in the presence of copper turnings for a quantitative conversion of barite sulfur to SO_2 offline prior to sulfur stable isotope measurements.

Pyrite sulfur was extracted using the chromium reduction method (Canfield et al., 1986). Pyrite extractions were carried out in 20 ml of concentrated HCl mixed with 40 ml of 1-M chromous chloride solutions for 2 h while heated under an N_2 atmosphere. The pyrite sulfur was

collected as silver sulfide in a silver nitrate trap and weighed to determine pyrite sulfur concentrations. Isotopic determinations were performed on a Finnigan MAT 251 mass spectrometer at CUG or a ThermoFinnigan Delta V continuous-flow isotope ratio mass spectrometer at the University of California-Riverside. Results are expressed in standard delta notation ($\delta^{34}S$) as per mille deviations versus the Vienna Canyon Diablo Troilite (VCDT) standard. Data quality was monitored via repeated analysis of two international standards, NBS 127 ($\delta^{34}S = +20.3‰$) and IAEA SO-5 ($\delta^{34}S = +0.5‰$), which yielded analytical precisions (2σ) of better than ± 0.3‰ for both CAS and pyrite $\delta^{34}S$ determinations.

3.2.3. Iron speciation analysis

Iron speciation analysis was undertaken following the protocol of Poulton and Canfield (2005). Sequential chemical extractions were used to separate sedimentary iron into different highly reactive (Fe_{HR}) pools: iron oxides (Fe_{ox}), magnetite (Fe_{mag}), carbonate-associated iron phases (Fe_{carb}), and pyrite (Fe_{py}). By definition, these pools are each readily reactive with hydrogen sulfide on short diagenetic time scales. First, sodium acetate was used to extract Fe_{carb}, then dithionite to extract Fe_{ox}, and lastly ammonium oxalate to extract Fe_{mag}. The concentrations of these Fe species were measured with a Perkin-Elmer DRC-e inductively coupled plasma mass spectrometer (ICP-MS) at CUG. Fe_{py} content was calculated based on pyrite sulfur concentrations from the chromium reduction analysis (above) assuming pyrite stoichiometry. Total iron (Fe_T) was determined by ICP-MS after chemical digestion. Analytical precision was better than ± 5% for Fe concentrations based on replicate analyses of extractions at all steps. The non-reactive Fe fraction was determined by difference, i.e., Fe_T minus Fe_{HR}.

3.2.4. Pyrite framboid sizes

Size distributions of pyrite framboids were determined for 7 of the 18 BMU samples and 11 of the 27 non-BMU samples. In general, the BMU samples contained many (i.e., hundreds) of framboids, whereas the non-BMU samples yielded few or zero framboids, although some contained euhedral pyrite crystals. The diameters of a total of 1098 framboids in 7 samples were measured in polished thin sections (cf. Wilkin et al., 1996) using a FEI Quanta 200 scanning electron microscope (SEM) at CUG. Framboidal and euhedral pyrite were easily distinguished under SEM, and the size and morphology of each pyrite crystal was recorded. For each sample, a minimum of 100 pyrite framboids were measured in order to achieve a statistically robust size distribution.

3.3. Results

The results of elemental and isotopic measurements for the full 60-m-thick Smithian-Spathian study section are given in Table S1, and additional data (e.g., pyrite framboid sizes) for the 3.6-m-thick BMU interval are given in Table S2. Chemostratigraphic profiles for the full section are shown in Fig. 4, and profiles for the BMU are shown in Fig. 5. Details of the Fe-speciation analysis are shown in Figs. 4-6 and a standard pyrite framboid plot for redox interpretations is shown in Fig. 7.

Total organic carbon (TOC) is low (mean 0.12%; max. 0.21%) except for the 3.6-m-thick BMU, in which TOC averaged 0.7% (max. 1.8%; Fig. 4A). The calcium carbonate fraction of the samples, which consists mainly of micrite, ranges from 0 to 96% (Table S1). The carbonate contents ($CaCO_3$) average 37 ± 27% in the BMU and 62 ± 26% in the non-BMU beds, reflecting the dominantly limestone composition of the latter. The $\delta^{13}C_{carb}$ profile shows ^{13}C-depleted values ranging from ca. –6‰ to −2‰ at 0–40 m (Smithian) and from ca. +2‰ to +4‰ at 48–60 m (Spathian) without systematic stratigraphic variation in either of these intervals (Fig. 4B). In contrast, the SSB interval at 40–48 m exhibits a rapid unidirectional shift in $\delta^{13}C_{carb}$ from ca. –4‰ to +4‰ that begins at the base of the BMU and extends ~4 m into the overlying Nanlinghu Formation. The largest part of this +8‰ isotopic shift is confined to the BMU.

The non-BMU beds yield Fe_{HR}/Fe_T values uniformly < 0.4 and Fe_{py}/Fe_{HR} values mostly < 0.3 (Fig. 4C-D). For the BMU, Fe_{HR}/Fe_T ratios are mostly > 0.4 (17 out of 18 samples), with higher Fe_{py}/Fe_{HR} values (> 0.7) associated with the carbonate-poor samples (< 50% $CaCO_3$) and somewhat lower values (0.4–0.8) with the carbonate-rich samples (> 50% $CaCO_3$) (Fig. 6). On a Fe_{py}/Fe_{HR} vs. Fe_{HR}/Fe_T crossplot, all non-BMU samples fall in the oxic-dysoxic field, and most BMU samples fall in the anoxic field, with carbonate-poor samples being euxinic and carbonate-rich samples being ferruginous (Fig. 6). Total Fe is significantly higher in the BMU beds (2.3 ± 1.6%) relative to the non-BMU beds (1.3 ± 1.1%) (Fig. 4E).

The $\delta^{34}S_{CAS}$ profile shows variation from +26‰ to +46‰ in the study section (Fig. 4F). The upper Smithian (at ~26–40 m) is characterized by a gradual negative shift in $\delta^{34}S_{CAS}$ from ~ +35‰ to +26‰, followed by a rapid positive shift from ~ +30‰ to +44‰ through the SSB interval (at 40–48 m). The lower Spathian exhibits relatively stable $\delta^{34}S_{CAS}$ values of +40‰ to +45‰ (except for a single-point outlier at +29‰).

The BMU samples yielded $\delta^{34}S_{py}$ ranging from −13.8‰ to +1.5‰ (Fig. 5A). The most ^{34}S-depleted values are associated with the samples yielding the highest Fe_{py}/Fe_{HR} and Fe_{HR}/Fe_T ratios (Fig. 5B-C). Pyrite framboids are found at highest concentrations from 0.3 to 2.2 m above the base of the BMU but are also present in some limestone samples from the base of the Nanlinghu Formation (Fig. 5D, Table S2). Greater than 90% of framboids in the BMU are < 5 μm, with a distinct size minimum (mean diameter = 3.5 ± 1.1 μm) at ~0.5–1.0 m. Samples from the base and top of the BMU (SM-20 and SM-36) yielded lower concentrations of framboids, which were characterized by a larger mean diameter (4.9–7.4 μm) and broader size range (Fig. 5D). Eleven non-BMU samples were examined for framboidal pyrite (5 from below and 6 from above the BMU), but only a single sample yielded a few framboids (SM-39, a limestone directly overlying the BMU; Fig. 5E), confirming that non-BMU samples accumulated under non-euxinic conditions. On a mean diameter vs. mean standard deviation crossplot, five of seven samples plot in the euxinic field and one sample falls on the threshold line (Fig. 7). There is no relationship between the size parameters of pyrite framboids and the number of framboids measured (Table S2), so normalization to a uniform number of measurements was deemed unnecessary.

4. Discussion

4.1. Increased organic carbon burial during the SSB interval

The South Majiashan section exhibits a large increase in TOC within the BMU straddling the SSB (mean 0.7%, max. 1.8%) relative to background sediments before and after this event (mean 0.12%; max. 0.21%; Fig. 4A). Globally, many areas show increases in sediment TOC during the SSB interval, e.g., the Nanpanjiang Basin (southwestern South China; Galfetti et al., 2007a, 2008; Sun et al., 2015), Vietnam (Komatsu et al., 2014), Arctic Canada (Grasby et al., 2013), and the western USA basin (Caravaca et al., 2017; Grosjean et al., 2018). Although the estimated pre-burial TOC content of the South Majiashan section was modest (~1–2%), increases in organic carbon burial over wide areas of seafloor globally during the SSB interval would potentially account for observed ~ +3 to +8‰ $\delta^{13}C_{carb}$ shifts in SSB profiles (Fig. 2).

4.2. Coupling of carbon and sulfur cycles during the SSB interval

4.2.1. South Majiashan

Carbonate C-isotope ($\delta^{13}C_{carb}$) and carbonate-associated sulfate S-isotope ($\delta^{34}S_{CAS}$) records are generally proxies for global-scale processes, and parallel shifts in $\delta^{13}C_{carb}$ and $\delta^{34}S_{CAS}$ profiles can

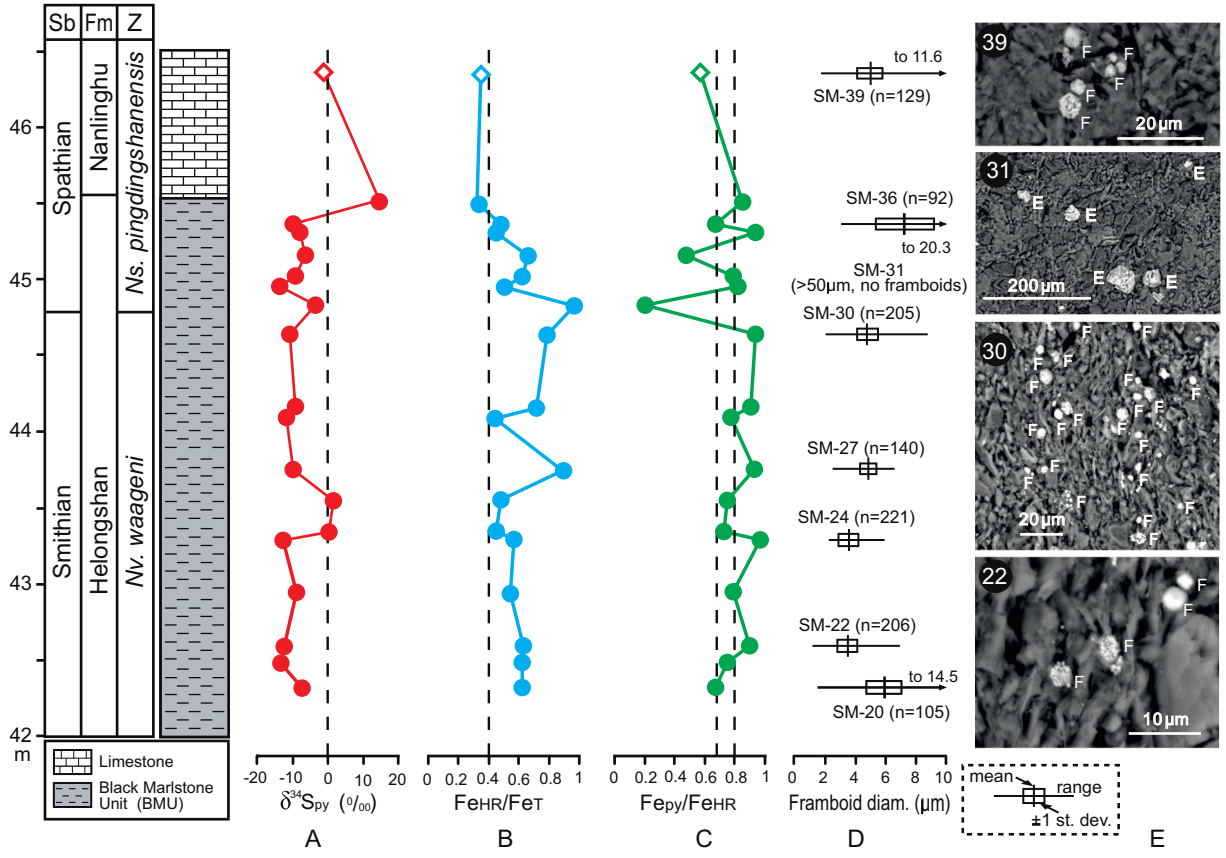

Fig. 5. Chemostratigraphy of the BMU interval at South Majiashan: (A) pyrite $\delta^{34}S$, (B) Fe_{HR}/Fe_T, (C) Fe_{py}/Fe_{HR}, (D) framboidal pyrite size distributions (legend at top), and (E) scanning electron microscope images (identified by sample number). Py = pyrite, E = euhedral, F = framboidal; other abbreviations and details as in Figs. 1, 2 and 4.

demonstrate close linkage of the marine carbon and sulfur cycles (Gill et al., 2007; Yan et al., 2009). Positive covariation of $\delta^{13}C_{carb}$ and $\delta^{34}S_{CAS}$ is a nearly ubiquitous feature of Lower Triassic sections persisting from the PTB (Luo et al., 2010) to the late Spathian (Song et al., 2014a, their figure 6). The present South Majiashan study section exhibits strong positive covariation, with $\delta^{13}C_{carb}$ and $\delta^{34}S_{CAS}$ simultaneously increasing by +8‰ and +15‰, respectively, over the limited 8-m interval straddling the SSB (Fig. 4).

Although potentially subject to multiple influences, concurrent positive excursions in $\delta^{13}C_{carb}$ and $\delta^{34}S_{CAS}$ at geologically short timescales

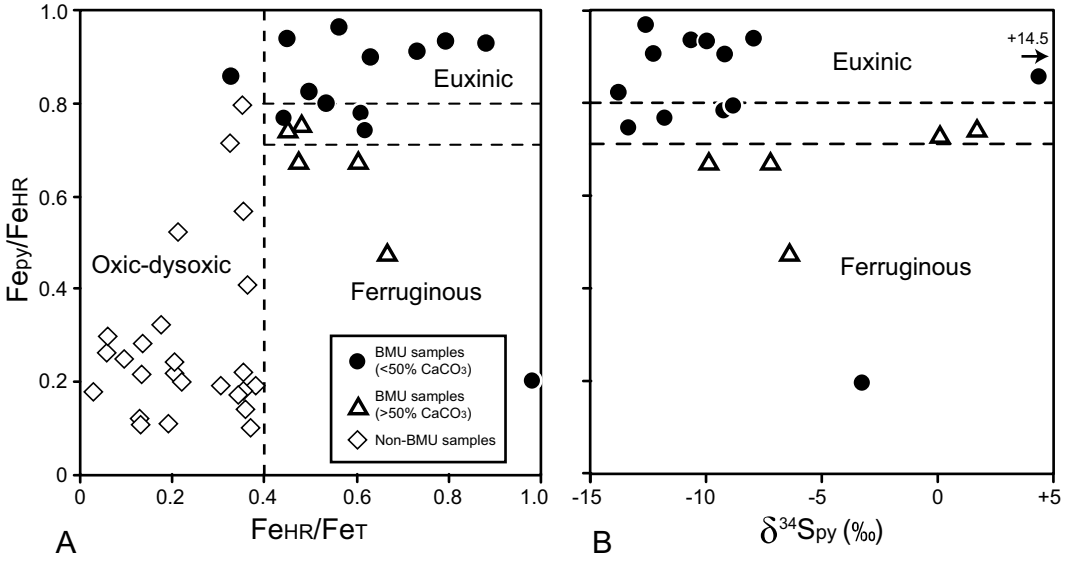

Fig. 6. Fe_{py}/Fe_{HR} versus (A) Fe_{HR}/Fe_T and (B) $\delta^{34}S_{py}$. Filled circles and open triangles represent BMU samples containing < 50% and > 50% $CaCO_3$, respectively; open diamonds represent limestone samples from below and above the BMU. Redox boundaries from Poulton and Canfield (2011); dashed lines at 0.7–0.8 for Fe_{py}/Fe_{HR} indicate uncertainty in position of euxinic/ferruginous boundary.

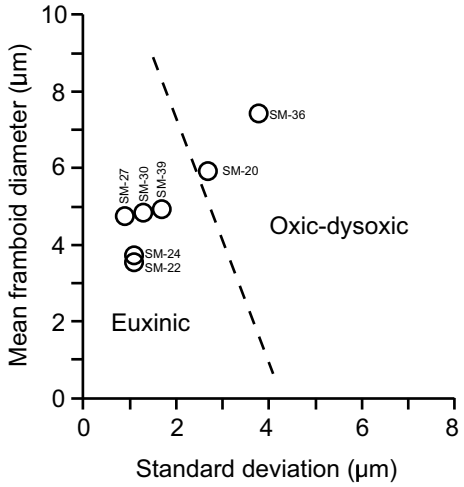

Fig. 7. Mean diameter versus standard deviation of pyrite framboid sizes for the BMU. The dashed line separating euxinic/anoxic from dysoxic facies is from Bond and Wignall (2010).

(~ < 1 Myr) are most readily explained by enhanced co-burial of ^{13}C-depleted organic carbon and ^{34}S-depleted pyrite at a global scale (Luo et al., 2010; Song et al., 2014a). Owing to preferential utilization of the light isotope of carbon (^{12}C) in photosynthesis and the light isotope of sulfur (^{32}S) by sulfate-reducing microbes during anaerobic decay of organic matter, enhanced co-burial of organic matter and pyrite leads to higher values for the $\delta^{13}C$ of dissolved inorganic carbon (DIC) and the $\delta^{34}S$ of sulfate in seawater. Parallel excursions of $\delta^{13}C_{carb}$ and $\delta^{34}S_{CAS}$ are a feature of many event intervals in Earth history, including the Late Cambrian OAE (Gill et al., 2011a); Jurassic Toarcian OAE (Gill et al., 2011b), some Cretaceous OAEs (Owens et al., 2013). In contrast to the short-term positive covariation of $\delta^{13}C_{carb}$ and $\delta^{34}S_{CAS}$ that reflects carbon-sulfur-cycle coupling via co-burial of organic carbon and pyrite (both reduced phases), the need for redox balance (i.e., approximate net charge neutrality) among all components of the exogenic system that are oxidizable/reducible generates a negative $\delta^{13}C_{carb}$-$\delta^{34}S_{CAS}$ coupling at longer timescales (> 10 Myr; Veizer et al., 1980; Walker, 1986). For this reason, the parallel excursions of $\delta^{13}C_{carb}$ and $\delta^{34}S_{CAS}$ developed during event intervals such as the SSB interval are fundamentally a short-term feature of chemostratigraphic records.

4.2.2. Comparison with other SSB sections

Nearly all SSB sections globally show significant shifts in $\delta^{13}C_{carb}$ and some also show $\delta^{34}S_{CAS}$ excursions through the SSB interval, although the covariation patterns are spatially variable. The Jesmond section in the Cache Creek Terrane, British Columbia (Panthalassic Ocean; Stebbins et al., 2018a), the Mineral Mountains section in Utah, western USA (Panthalassic Ocean; Thomazo et al., 2018), and the Mud section in the Spiti Valley, India (southern Neo-Tethys Ocean, Stebbins et al., 2018b) all show parallel positive $\delta^{13}C_{carb}$ and $\delta^{34}S_{CAS}$ excursions through the SSB interval (Fig. 8). On the other hand, the Shitouzhai section (shallow margin of Nanpanjiang Basin in South China, Guizhou Province) shows a positive $\delta^{13}C_{carb}$ shift (+4‰) but a more complex pattern of $\delta^{34}S_{CAS}$ variation (Fig. 8E; Zhang et al., 2015). At Shitouzhai, the overall pattern is one of negative $\delta^{13}C_{carb}$-$\delta^{34}S_{CAS}$ covariation, with a modest relationship for the section as a whole ($r = -0.38$; p ~0.08, $n = 15$; Fig. 9).

The South Majiashan and Shitouzhai sections show similar $\delta^{13}C_{carb}$ (~ −3 to −2‰) and $\delta^{34}S_{CAS}$ (~ +30 to +35‰) in the middle Smithian (Fig. 8). During the SSB interval, these sections show divergent patterns: both are characterized by increasing $\delta^{13}C_{carb}$ (rising to ~ +1‰ at South Majiashan and to +4‰ at Shitouzhai), but $\delta^{34}S_{CAS}$ increases at South Majiashan (rising to ~ +40 to +50‰) while decreasing at Shitouzhai (decreasing to ~ +23 to +27‰). This divergence leads to opposite correlations for the SSB interval, with South Majiashan exhibiting a positive $\delta^{13}C$-$\delta^{34}S$ correlation and Shitouzhai a negative one (Fig. 9). We interpret the similar pre-SSB values to represent the isotopic composition of seawater DIC and sulfate prior to the SSB event. During the SSB interval, the common shift in $\delta^{13}C_{carb}$ reflects increasing seawater $\delta^{13}C_{DIC}$ linked to a global increase in the organic carbon burial flux (Fig. 10A-B), and the rise in $\delta^{34}S_{CAS}$ at South Majiashan is consistent with increasing seawater sulfate $\delta^{34}S$ driven by enhanced microbial sulfate reduction (MSR) linked to organic carbon burial (note that SSB sections from other cratons also show this pattern; Fig. 8). Positive short-term covariation of $\delta^{13}C_{carb}$ and $\delta^{34}S_{CAS}$ is a common pattern reflecting global-scale co-burial of reduced carbon and sulfur (i.e., organic matter and pyrite) (Gill et al., 2007; Yan et al., 2009; Luo et al., 2010; Song et al., 2014a).

From this perspective, the negative $\delta^{34}S_{CAS}$ shift at Shitouzhai during the SSB interval (Fig. 9) is anomalous and likely to have been the result of the local evolution of watermass chemistry (Zhang et al., 2015). The Nanpanjiang Basin is considered to have been unrestricted and fully marine in terms of its watermass chemistry (Lehrmann et al., 2003; Song et al., 2014a), so changes in sulfate concentrations due to basinal restriction and/or brackish conditions (Algeo et al., 2015) appear unlikely. However, the location of Shitouzhai within the inner Nanpanjiang Basin, on the southern margin of the Yangtze Platform, may have been an important factor influencing local watermass dynamics. Deep cratonic shelves on open continental margins are commonly subject to strong upwelling in their inner reaches, where waters are forced abruptly upward by topographic barriers. This situation existed in the Permian Phosphoria Sea (Piper and Link, 2002) and a variation of it is present in the Modern Baltic Sea (despite its shallow outer bounding sill), where an abrupt shallowing from the Baltic Proper into the Bothian Gulf forces large-scale upwelling of nutrient-rich deepwaters (Rahm and Danielsson, 2007). We hypothesize that large-scale upwelling along the inner (northern) margin of the Nanpanjiang Basin resulted in introduction of large quantities of deepwater H_2S that was oxidized in the ocean-surface layer (Fig. 10B-C). This H_2S was ^{34}S-depleted owing to generation through microbial sulfate reduction (MSR) in deep anoxic waters of the Nanpanjiang Basin. A corollary to this hypothesis is that seawater sulfate concentrations must have been low during the SSB event in order to allow regional heterogeneity in sulfate $\delta^{34}S$ to develop. Estimates of seawater [SO_4^{2-}] during the Early Triassic are indeed low, ranging from < 4 mM (Luo et al., 2010; Song et al., 2014a) to ~2–9 mM (Stebbins et al., 2018a).

4.3. Ocean-redox changes during the SSB interval

4.3.1. South Majiashan

Fe speciation and pyrite S-isotope data provide information about local redox conditions (although possibly reflecting broader redox trends). Iron is highly sensitive to dissolved oxygen levels and the presence or absence of hydrogen sulfide in aqueous systems, and the ratios of various Fe species have been used to reconstruct local redox variation in modern and ancient marine environments (e.g., Lyons and Severmann, 2006; Poulton and Canfield, 2011). Sediment Fe_{HR}/Fe_T ratios average ~0.2 in well-oxygenated settings but rise under more reducing conditions, with 0.38 as the conventional threshold between oxic and anoxic facies. On the basis of Fe_{py}/Fe_{HR} ratios, anoxic environments can be further distinguished as either ferruginous (< 0.7–0.8) or euxinic (> 0.7–0.8; Fig. 6A).

Several caveats apply to use of Fe-speciation data as a redox proxy. First, Fe-system proxies do not necessarily yield accurate redox interpretations for low-Fe carbonate sediments, and a threshold of Fe_T > 0.5% has been recommended (Clarkson et al., 2014). At South Majiashan, all samples from both the BMU and non-BMU beds have Fe_T > 0.5%, and Fe_{HR}/Fe_T shows no relationship to either $CaCO_3$ or Fe_T content (Fig. S2). Second, the effectiveness of Fe-speciation data as

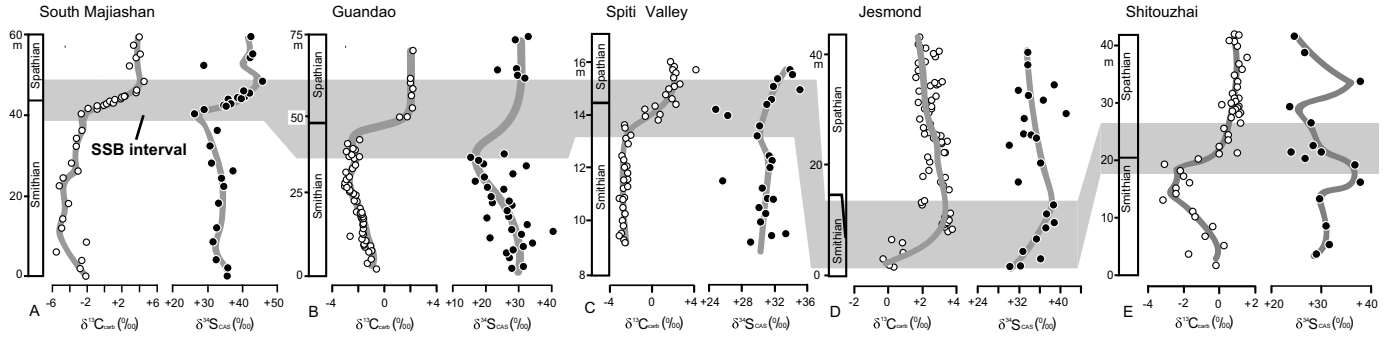

Fig. 8. Global comparison of $\delta^{13}C_{carb}$ and $\delta^{34}S_{CAS}$ profiles for (A) South Majiashan (this study), (B) Guandao (Song et al., 2014a), (C) Spiti Valley (Stebbins et al., 2018b); (D) Jesmond (Stebbins et al., 2018a), (E) Shitouzhai (Zhang et al., 2015).

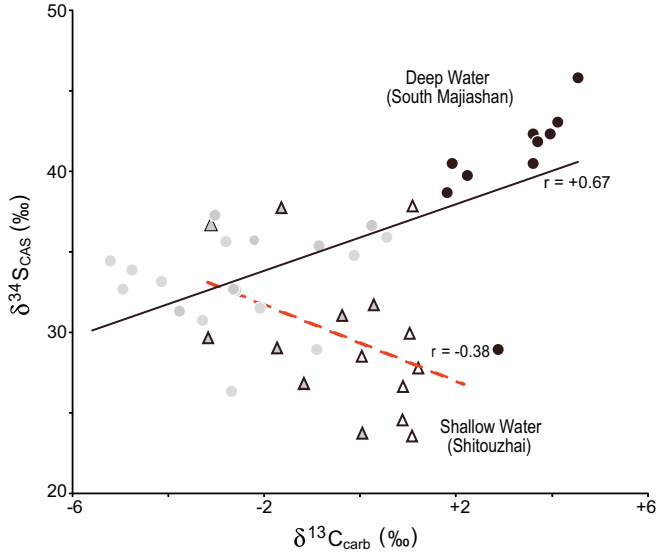

Fig. 9. Comparison of $\delta^{13}C_{carb}$-$\delta^{34}S_{CAS}$ covariation for South Majiashan (this study) and Shitouzhai (Zhang et al., 2015). The South Majiashan section exhibits a strong positive correlation ($r = +0.67$, $p < 0.01$, $n = 28$); Smithian samples (gray circles) and Spathian samples (black circles) are roughly colinear. The Shitouzhai section exhibits a moderate negative correlation ($r = -0.38$, $p \sim 0.08$, $n = 15$); Smithian samples (gray triangles) and Spathian samples (white triangles) both exhibit considerable scatter.

a redox proxy diminishes at high accumulation rates ($> 1000\,g\,m^{-2}\,yr^{-1}$) owing to siliciclastic dilution (Lyons and Severmann, 2006). However, bulk accumulation rates for the study section were no more than $\sim 260\,g\,m^{-2}\,yr^{-1}$ based on an average sedimentation rate of 105 m Myr^{-1} and an assumed bulk density of $2.5\,g\,cm^{-3}$, and even lower if the BMU represents a stratigraphically condensed interval (see Section 3.1). These observations suggest that redox interpretations based on Fe-speciation data are robust for both the BMU and non-BMU samples at South Majiashan.

Fe speciation data for South Majiashan demonstrate significant redox changes around the SSB interval (Figs. 4-6). High values of Fe_{HR}/Fe_T (0.63 ± 0.19) and Fe_{py}/Fe_{HR} (0.87 ± 0.08) for the carbonate-poor BMU samples ($n = 18$) imply euxinic conditions. These samples accumulated in a severely Fe-limited system—an inference that is supported by the strong correlation of Fe_{py} with Fe_{HR} (Fig. S3). The only exception is a single sample (SM-31) yielding high Fe_{HR}/Fe_T (0.97) but low Fe_{py}/Fe_{HR} (0.20), suggesting ferruginous rather than euxinic conditions. The lower mean Fe_{HR}/Fe_T (0.51 ± 0.11) and Fe_{py}/Fe_{HR} (0.67 ± 0.11) for the carbonate-rich BMU samples suggest less intense and/or more intermittent euxinic conditions. Non-BMU samples exhibit even lower mean Fe_{HR}/Fe_T (0.26 ± 0.13) and Fe_{py}/Fe_{HR} (0.31 ± 0.21), consistent with oxic-dysoxic conditions (Fig. 6). Thus, the BMU represents an interval of euxinic sedimentation in an area that otherwise experienced mainly oxic-dysoxic conditions throughout the Smithian and early Spathian substages of the Lower Triassic.

The redox interpretations based on Fe speciation data are supported by pyrite framboid size distributions and $\delta^{34}S_{py}$ compositions. In euxinic facies, such as the modern Black Sea, pyrite framboid diameters are small (mostly < 7 μm) and show a narrow size distribution (as reflected in the standard deviation of framboid diameters) (Wilkin et al., 1996). In contrast, framboids that form in sediments underlying oxygenated waters are characterized by larger diameters and a broader size distribution (Wilkin and Arthur, 2001; Bond and Wignall, 2010). At South Majiashan, large concentrations of small framboids (< 5 μm; Fig. 5E) are consistent with the existence of water-column euxinia during BMU deposition. Ten of the 12 carbonate-poor BMU samples interpreted as euxinic based on Fe systematics yield strongly ^{34}S-depleted pyrite S-isotope compositions (−10.9 ± 1.9‰; Fig. 5A). In contrast, the seven carbonate-rich BMU samples exhibit higher and more variable $\delta^{34}S_{py}$ values (−4.6 ± 4.6‰; Fig. 5A), consistent with a larger fraction of pyrite formed in the sediment and, thus, deposition of these samples under less intensely reducing conditions.

The degree of S-isotope fractionation associated with microbial sulfate reduction (MSR) in the SSB beds at South Majiashan is also consistent with a euxinic water column. S-isotope analysis of marine evaporites and CAS indicates that seawater sulfate $\delta^{34}S$ during the Olenekian was ca. +31‰ (Kampschulte and Strauss, 2004), which is consistent with our $\delta^{34}S_{CAS}$ data (Fig. 5). Fractionation between seawater sulfate and pyrite ($\Delta\delta^{34}S_{CAS\text{-}py}$) thus ranged from ~40 to 45‰ for the carbonate-poor BMU samples, similar to values reported for a number of Upper Permian-Lower Triassic sections (e.g., Nielsen and Shen, 2004; Algeo et al., 2008, 2011b; Stebbins et al., 2018a, 2018b). These values are typical of MSR in a euxinic water column (Canfield, 1997; Algeo et al., 2015), although fractionations closer to 60‰ have been reported in some modern euxinic environments (e.g., the Black Sea; Wilkin and Arthur, 2001). Smaller and more variable $\Delta\delta^{34}S_{CAS\text{-}py}$ values for the carbonate-rich BMU samples (~33 to 45‰) are consistent with MSR in a partially closed porewater system with a modest degree of Rayleigh distillation of sulfate (Wilkin and Arthur, 2001; Algeo et al., 2015).

4.3.2. Comparison with other SSB sections

Previous studies have documented redox changes during the Smithian to early Spathian by means of geochemical and sedimentary proxies (Galfetti et al., 2007a; Song et al., 2012; Grasby et al., 2013; Tian et al., 2014; Wei et al., 2015; Zhang et al., 2015; Clarkson et al., 2016; Lau et al., 2016; Huang et al., 2017). Widespread oceanic anoxia appears to have developed in two stages during this interval: (1) the first OAE occurred preceding and/or coinciding with the N3 $\delta^{13}C$ minimum (i.e., near the middle/late Smithian boundary; see Zhang et al., 2019) and is here termed the "mid-Smithian-OAE", and (2) the

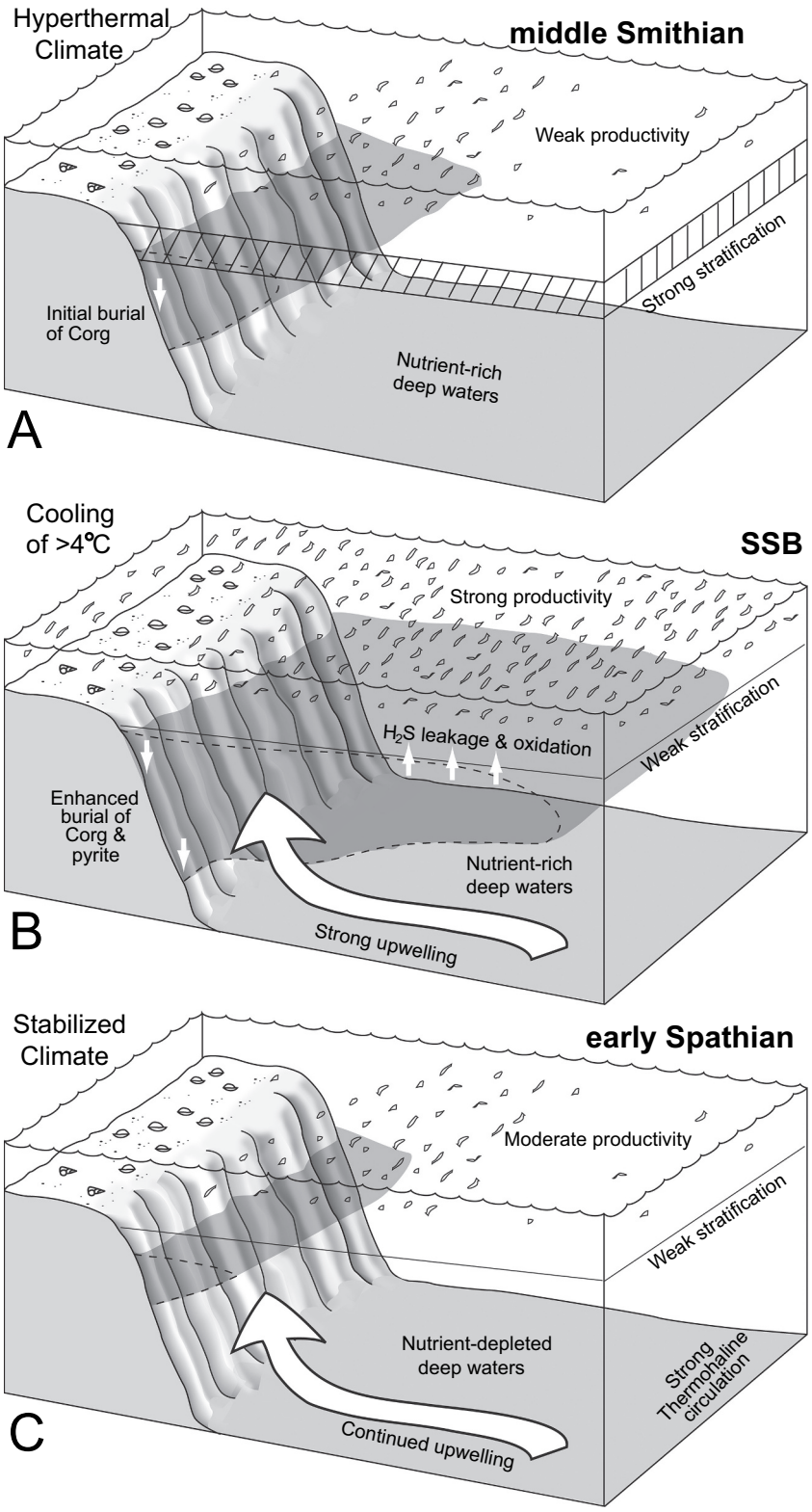

Fig. 10. Paleoceanographic model of the marine upwelling system on the western margin of the South China Craton during (A) middle Smithian, (B) Smithian-Spathian boundary (SSB), and (C) early Spathian. The model is based on re-invigoration of global-ocean thermohaline circulation as a consequence of strong climatic cooling at the SSB. Intensified upwelling flushed nutrients that had accumulated in the deep ocean during the Griesbachian-Smithian (an interval characterized by hyperwarming and strong water-column stratification; Sun et al., 2012; Song et al., 2013b, Song et al., 2014a) into the surface layer, stimulating marine productivity and BMU deposition. The model accounts for depth-related differences in $\delta^{13}C_{carb}$-$\delta^{34}S_{CAS}$ covariation: deep-water sections such as South Majiashan exhibit positive covariation owing to enhanced co-burial of organic carbon and pyrite, and shallow-water sections such as Shitouzhai exhibit negative covariation owing to a local increase in $\delta^{13}C_{DIC}$ owing to enhanced productivity and a concurrent decrease in $\delta^{34}S_{sulfate}$ owing to oxidation of upwelled H_2S. See text for further explanation.

second OAE occurred during the SSB interval, coinciding with the $\delta^{13}C$ shift between the N3 minimum and subsequent P3 maximum (i.e., from the *Anasibirites multiformis* beds up to the Tirolitid n. gen. A beds in South China; see Galfetti et al., 2007a) and is here termed the "SSB-OAE" (Fig. 2).

The mid-Smithian-OAE has been recognized in multiple regions globally using various types of geological evidence. It has been documented in the Arctic Canada (Grasby et al., 2013) and on the Arabian Margin of the Neo-Tethys Ocean (Clarkson et al., 2016) based on C-S-Fe and Mo data. In South China, it has been recognized on the basis of Ce* and Th/U ratios of conodont apatite (Song et al., 2012) and pyrite framboid size distributions (Tian et al., 2014) from the Nanpanjiang Basin, and Mo and U enrichments in shaly successions at Chaohu on the northern Yangtze Platform (Wei et al., 2015). However, other studies in South China have inferred largely oxic-dysoxic conditions during the mid-Smithian, as based on framboidal pyrite and Fe speciation data

from Chaohu (Huang et al., 2017; this study). The inconsistent results for the Chaohu sections may be due to differences in proxy response, sample density, or lithology. In the present study, our samples have relatively high carbonate and low Fe contents, predisposing them to yield a less reducing signal than the shalier sections studied by Wei et al. (2015).

Despite evidence for a separate SSB-OAE, it has been regarded as the same as the Smithian-OAE in most previous studies (Song et al., 2012; Grasby et al., 2013; Tian et al., 2014; Wei et al., 2015). In these studies, mid-Smithian oceanic anoxia has been attributed exclusively to extreme greenhouse conditions (Song et al., 2012; Grasby et al., 2013; Tian et al., 2014). The failure to recognized a separate SSB-OAE event has been due, in part, to stratigraphic placement of the SSB at too low a level in key conodont $\delta^{18}O$ studies (i.e., Sun et al., 2012), leading to the view that the SSB coincided with the Smithian hyperwarming event, rather than with the subsequent cooling (see review by Zhang et al. (2019). Several studies have provided evidence of a separate SSB-OAE in sections in China (Galfetti et al., 2007a; Tian et al., 2014; Huang et al., 2017), southern Tethys (Galfetti et al., 2008), Arctic Canada (Grasby et al., 2013), and the Arabian Margin of the Neotethys (Clarkson et al., 2016), although only the last-named study specifically recognized the SSB-OAE as an event separate from the middle Smithian event. In addition, positive excursions of both carbon and sulfur isotope profiles during the SSB interval imply that this OAE was likely a global event (Stebbins et al., 2018a, 2018b; this study). Nonetheless, some sections have yielded evidence of locally oxic or dysoxic conditions during the SSB interval, including Tulong in South Tibet (Brühwiler et al., 2009) and Shitouzhai in the Nanpanjiang Basin (Zhang et al., 2015). This may reflect expansion of oceanic anoxia in the thermocline region with little impact on shallow facies (Clarkson et al., 2016).

4.4. Cooling-driven oceanic anoxia during the SSB interval

The pattern and causes of oceanic anoxia during the Early Triassic generally, and during the SSB interval specifically, remain controversial, although extreme global warming (i.e., the “Smithian Thermal Maximum”; Zhang et al., 2019) is likely to have played a role. Climatic warming lowers the density of the ocean-surface layer, intensifying water-column stratification (Song et al., 2013a), and reduces the solubility of oxygen in seawater (Keeling et al., 2010; Fig. 10A). Additionally, warmer temperatures may lead to enhanced marine productivity and benthic oxygen demand through higher weathering rates and riverine nutrient fluxes (Algeo and Twitchett, 2010). The cause of oceanic environmental changes during the middle Smithian is uncertain, although recent work using Hg concentrations as a volcanic proxy has demonstrated globally high values from the late Changhsingian to the late Smithian, followed by a sharp decline at the SSB (Shen et al., 2019). This pattern is consistent with moderately intense volcanism (or magmatism) likely linked to the Siberian Traps Large Igneous Province throughout the first ~1.5 Myr of the Early Triassic, followed by a sharp reduction in this activity around the SSB (Shen et al., 2019).

In contrast to this general model of hyperwarming-driven anoxia during the middle Smithian (and much of the Early Triassic up to that time), the development of oceanic anoxia during the SSB interval may have been caused by a completely different mechanism. Key differences are that the SSB event was associated with (1) massive organic carbon burial, as reflected in large (~6‰) positive excursions of both $\delta^{13}C_{carb}$ and $\delta^{13}C_{org}$ (Fig. 1; Payne et al., 2004; Galfetti et al., 2007b; Tong et al., 2007; Meyer et al., 2013; Grasby et al., 2013), and (2) strong climatic cooling, due to the attendant drawdown of atmospheric CO_2 levels through organic carbon burial, as reflected in conodont $\delta^{18}O$ records (Sun et al., 2012; Romano et al., 2013; Fig. 1). Although tropical SSTs of the Spathian remained warm (~32 °C) compared to those of the modern ocean (~28 °C), the SSB marked the termination of the hyper-greenhouse conditions of the middle Smithian, when SSTs were potentially as high as ~40 °C in the tropics.

Here, we propose a mechanism for the SSB ocean anoxic event based on global climatic cooling. In this scenario, cooling caused a reinvigoration of oceanic thermohaline circulation, locally enhancing upwelling of nutrient-rich deep waters and increasing marine productivity and organic carbon sinking fluxes (Fig. 10). A transient increase in marine productivity was thus an important factor in the expansion of oceanic oxygen-minimum zones during the SSB event (Algeo et al., 2010, 2011b). Because oceanic anoxia at the SSB was probably associated with stronger oceanic thermohaline circulation and, thus, improved deepwater ventilation, it is unlikely to have been global or near-global in extent (see Section 2.3). Rather, the effects of stronger oceanic circulation are likely to have been felt primarily in upwelling zones located on the western margins of continents such as South China (this study) and northwestern Pangea (Grasby et al., 2013).

Evidence for reduced oceanic stratification, increased deepwater ventilation, and enhanced upwelling at the SSB has been documented in several recent studies. Water-column stratification is closely linked to vertical $\delta^{13}C_{DIC}$ gradients as a consequence of transfer of isotopically light column to the deep watermass via the biological pump (Rind, 1998). A collapse in the vertical $\delta^{13}C_{DIC}$ gradient at the SSB (Song et al., 2013b) is thus evidence of a shift from a strongly stratified ocean to one with more vigorous thermohaline circulation. Increased deep-ocean ventilation during the Spathian (Fig. 10C) is evidenced by the wide occurrence of oxidized, red pelagic clays in the Panthalassa Ocean (Japan) and reddish carbonates in the Tethys Ocean (South China and Tibet) (Brühwiler et al., 2009; Takahashi et al., 2009). Upwelling intensity can be proxied by extended tricyclic terpane ratios (ETR), with values > 4 indicative of strong upwelling (Saito et al., 2013). At South Majiashan, ETRs are mostly < 2 throughout the Lower Triassic except for the SSB interval, where several peaks > 4 provide evidence of upwelling events (Fig. 1; Saito et al., 2013). These oceanographic changes are consistent with an invigoration of thermohaline circulation triggered by strong cooling (> 4 °C) at the SSB (Fig. 1; Sun et al., 2012).

One important aspect of our hypothesis is that the SSB cooling event, once initiated, would have been self-sustaining for the duration of the event owing to a positive climate feedback. Initial increases in marine productivity and organic carbon burial triggered by this event would have progressively lowered atmospheric CO_2 levels, enhancing the cooling trend and, thus, the thermohaline overturning circulation of the oceans. The impetus for cooling would have persisted until the large nutrient inventories that had accumulated in the deep ocean during the ~1.5-Myr-long pre-SSB Early Triassic interval of stagnated ocean circulation were depleted (Fig. 10B-C). At that point, decreases in marine productivity and organic carbon burial rates and stabilization of atmospheric pCO_2 at levels below the middle Smithian maximum would have terminated the cooling trend. Although circumstantial, evidence for falling atmospheric pCO_2 during the SSB event includes (1) climatic cooling (Sun et al., 2012), and (2) reduced $\Delta^{13}C_{carb\text{-}org}$. Carbonate $\delta^{13}C$ profiles show shifts mostly ranging from +3 to +6‰ at the SSB (Figs. 4, 8; Payne et al., 2004; Tong et al., 2007; Galfetti et al., 2007b). The available $\delta^{13}C$ profiles for organic carbon all show shifts of ca. +6‰ (Galfetti et al., 2007b; Grasby et al., 2013), indicating a potential reduction in average $\Delta^{13}C_{carb\text{-}org}$ values of several per mille during the SSB event (but see Thomazo et al., 2016; Caravaca et al., 2017). $\Delta^{13}C_{carb\text{-}org}$ is a proxy for photosynthetic fractionation by marine algae, and reduced values are consistent with lower atmospheric pCO_2 levels (Rau et al., 1997).

5. Conclusions

This study investigated ocean anoxic events and their mechanisms from the middle Smithian to the early Spathian. The middle Smithian OAE (dating to the *Owenites koeneni* beds in South China, and coinciding with the N3 $\delta^{13}C$ minimum) was probably caused by late-stage magmatic activity of the Siberian Traps LIP, which triggered a sharp

temperature rise (the "Smithian Thermal Maximum") and injection of ^{13}C-depleted volcanogenic carbon into the global carbon cycle. In contrast, the SSB OAE coinciding with the N3-to-P3 $\delta^{13}C$ shift is hypothesized to have been linked to to global climatic cooling. At South Majiashan, on the western paleomargin of the South China Craton, the SSB OAE was associated with concurrent rapid positive shifts in the $\delta^{13}C_{carb}$ and $\delta^{34}S_{CAS}$ profiles, reflecting massive co-burial of organic carbon and pyrite during a geologically short (~120–200 kyr) euxinic episode linked to upwelling. Upwelling recycled nutrients sequestered in the deep ocean during a ~1.5-Myr-long interval of intense oceanic stratification in the early part of the Early Triassic, leading to increased marine productivity. The initial cooling was potentially sustained by a positive climate feedback related to organic carbon burial and declining atmospheric CO_2 levels, and it was finally terminated by the depletion of the excess nutrients in the deep ocean.

Acknowledgments

We thank Arnaud Brayard and André Strasser for editorial handling of the manuscript and two anonymous reviewers for helpful comments. This work was supported by the Natural Science Foundation of China (grants nos. 41872033; 41402302; 41530414; 41661134047), the Research Program the State Key Laboratory of Palaeobiology and Stratigraphy (143106), the Natural Science Foundation of Hubei (2017CFB610). Research by TJA was supported by the Sedimentary Geology and Paleobiology program of the U.S. National Science Foundation, the NASA Exobiology program, and the State Key Laboratory of Geological Processes and Mineral Resources, China University of Geosciences-Wuhan. JDO acknowledges support from Agouron, U.S. National Science Foundation and NASA Exobiology program. TWL acknowledges support from the U.S. National Science Foundation. This paper is a contribution to IGCP Projects 572 and 630.

Appendix A. Supplementary data

Supplementary data to this article can be found online at https://doi.org/10.1016/j.earscirev.2019.01.009.

References

Algeo, T.J., Twitchett, R.J., 2010. Anomalous Early Triassic sediment fluxes due to due to elevated weathering rates and their biological consequences. Geology 38, 1023–1026.

Algeo, T.J., Shen, Y., Zhang, T., Lyons, T.W., Bates, S.M., Rowe, H., Nguyen, T.K.T., 2008. Association of ^{34}S-depleted pyrite layers with negative carbonate $\delta^{13}C$ excursions at the Permian/Triassic boundary: evidence for upwelling of sulfidic deep-ocean watermasses. Geochem. Geophys. Geosyst. 9, Q04025.

Algeo, T.J., Hinnov, L., Moser, J., Maynard, J.B., Elswick, E., Kuwahara, K., Sano, H., 2010. Changes in productivity and redox conditions in the Panthalassic Ocean during the latest Permian. Geology 38, 187–190.

Algeo, T.J., Chen, Z.Q., Fraiser, M.L., Twitchett, R.J., 2011a. Terrestrial–marine teleconnections in the collapse and rebuilding of Early Triassic marine ecosystems. Palaeogeogr. Palaeoclimatol. Palaeoecol. 308, 1–11.

Algeo, T.J., Kuwahara, K., Sano, H., Bates, S., Lyons, T., Elswick, E., Hinnov, L., Ellwood, B., Moser, J., Maynard, J.B., 2011b. Spatial variation in sediment fluxes, redox conditions, and productivity in the Permian–Triassic Panthalassic Ocean. Palaeogeogr. Palaeoclimatol. Palaeoecol. 308 (1–2), 65–83.

Algeo, T.J., Henderson, C.M., Tong, J., Feng, Q., Yin, H., Tyson, R.V., 2013. Plankton and productivity during the Permian–Triassic boundary crisis: an analysis of organic carbon fluxes. Glob. Planet. Change 105, 52–67.

Algeo, T.J., Luo, G.M., Song, H.Y., Lyons, T.W., Canfield, D.E., 2015. Reconstruction of secular variation in seawater sulfate concentrations. Biogeosciences 12 (7), 2131–2151.

Berner, R.A., 2002. Examination of hypotheses for the Permo–Triassic boundary extinction by carbon cycle modeling. Proc. Natl. Acad. Sci. (U.S.A.) 99, 4172–4177.

Bond, D.P.G., Wignall, P.B., 2010. Pyrite framboid study of marine Permian-Triassic boundary sections: a complex anoxic event and its relationship to contemporaneous mass extinction. Geol. Soc. Am. Bull. 122, 1265–1279.

Bottjer, D.J., Clapham, M.E., Fraiser, M.L., Powers, C.M., 2008. Understanding mechanisms for the end-Permian mass extinction and the protracted Early Triassic aftermath and recovery. GSA Today 18, 4–10.

Brand, U., Posenato, R., Came, R., Affek, H., Angiolini, L., Azmy, K., Farabegoli, E., 2012. The end-Permian mass extinction: A rapid volcanic CO_2 and CH_4 climatic catastrophe. Chem. Geol. 322, 121–144.

Brayard, A., Bucher, H., Escarguel, G., Fluteau, F., Bourquin, S., Galfetti, T., 2006. The Early Triassic ammonoid recovery: Paleoclimatic significance of diversity gradients. Palaeogeogr. Palaeoclimatol. Palaeoecol. 239, 374–395.

Brayard, A., Escarguel, G., Bucher, H., 2007. The biogeography of Early Triassic ammonoid faunas: clusters, gradients, and networks. Geobios 40, 749–765.

Brayard, A., Escarguel, G., Bucher, H., Brühwiler, T., 2009. Smithian and Spathian (Early Triassic) ammonoid assemblages from terranes: Paleoceanographic and paleogeographic implications. J. Asian Earth Sci. 36, 420–433.

Brühwiler, T., Goudemand, N., Galfetti, T., Bucher, H., Baud, A., Ware, D., Hermann, E., Hochuli, P.A., Martini, R., 2009. The Lower Triassic sedimentary and carbon isotope records from Tulong (South Tibet) and their significance for Tethyan palaeoceanography. Sed. Geol. 222, 314–332.

Brühwiler, T., Bucher, H., Brayard, A., Goudemand, N., 2010. High-resolution biochronology and diversity dynamics of the Early Triassic ammonoid recovery: the Smithian faunas of the Northern Indian Margin. Palaeogeogr. Palaeoclimatol. Palaeoecol. 297, 491–501.

Burdett, J.W., Arthur, M.A., Richardson, M., 1989. A Neogene seawater sulfur isotope age curve from calcareous pelagic microfossils. Earth Planet. Sci. Lett. 94, 189–198.

Burgess, S.D., Muirhead, J.D., Bowring, S.A., 2017. Initial pulse of Siberian Traps sills as the trigger of the end-Permian mass extinction. Nat. Commun. 8, 164.

Canfield, D.E., Raiswell, R., Westrich, J.T., Reaves, C.M., Berner, R.A., 1986. The use of chromium reduction in the analysis of reduced inorganic sulfur in sediments and shales. Chem. Geol. 54, 149–155.

Caravaca, G., Thomazo, C., Vennin, E., Olivier, N., Coquerez, T., Escarguel, G., Fara, E., Jenks, J.F., Bylund, K.G., Stephen, D.A., 2017. Early Triassic fluctuations of the global carbon cycle: New evidence from paired carbon isotopes in the western USA basin. Glob. Planet. Change 154, 10–22.

Chen, Z.Q., Benton, M.J., 2012. The timing and pattern of biotic recovery following the end-Permian mass extinction. Nat. Geosci. 5, 375–383.

Chen, J., Shen, S., Li, X., Xu, Y., Joachimski, M.M., Bowring, S.A., Erwin, D.H., Yuan, D., Chen, B., Zhang, H., 2016. High-resolution SIMS oxygen isotope analysis on conodont apatite from South China and implications for the end-Permian mass extinction. Palaeogeogr. Palaeoclimatol. Palaeoecol. 448, 26–38.

Clarkson, M.O., Poulton, S.W., Guilbaud, R., Wood, R.A., 2014. Assessing the utility of Fe/Al and Fe-speciation to record water column redox conditions in carbonate-rich sediments. Chem. Geol. 382, 111–122.

Clarkson, M.O., Wood, R.A., Poulton, S.W., Richoz, S., Newton, R.J., Kasemann, S.A., Bowyer, F., Krystyn, L., 2016. Dynamic anoxic ferruginous conditions during the end-Permian mass extinction and recovery. Nat. Commun. 7, 12236.

Elrick, M., Polyak, V., Algeo, T.J., Romaniello, S., Asmerom, Y., Herrmann, A.D., Anbar, A.D., Zhao, L., Chen, Z.Q., 2017. Global-ocean redox variation during the middle-late Permian through Early Triassic based on uranium isotope and Th/U trends of marine carbonates. Geology 45 (2), 163–166.

Erwin, D.H., 1993. The Great Paleozoic Crisis: Life and Death in the Permian. Columbia University Press, pp. 327.

Feng, Z.Z., Bao, Z.D., Li, S.W., 1997. Lithofacies Paleogeography of Middle and Lower Triassic of South China. Petroleum Industry Press, Beijing, pp. 222 (in Chinese with English abstract).

Galfetti, T., Bucher, H., Ovtcharova, M., Schaltegger, U., Brayard, A., Brühwiler, T., Goudemand, N., Weissert, H., Hochuli, P.A., Cordey, F., Guodun, K., 2007a. Timing of the Early Triassic carbon cycle perturbations inferred from new U-Pb ages and ammonoid biochronozones. Earth Planet. Sci. Lett. 258, 593–604.

Galfetti, T., Hochuli, P.A., Brayard, A., Bucher, H., Weissert, H., Vigran, J.O., 2007b. Smithian-Spathian boundary event: Evidence for global climatic change in the wake of the end-Permian biotic crisis. Geology 35, 291–294.

Galfetti, T., Bucher, H., Martini, R., Hochuli, P.A., Weissert, H., Crasquin-Soleau, S., Brayard, A., Goudemand, N., Brühwiler, T., Kuang, G., 2008. Evolution of Early Triassic outer platform paleoenvironments in the Nanpanjiang Basin (South China) and their significance for the biotic recovery. Sed. Geol. 204, 36–60.

Gill, B.C., Lyons, T.W., Saltzman, M.R., 2007. Parallel, high-resolution carbon and sulfur isotope records of the evolving Paleozoic marine sulfur reservoir. Palaeogeogr. Palaeoclimatol. Palaeoecol. 256 (3–4), 156–173.

Gill, B.C., Lyons, T.W., Young, S.A., Kump, L.R., Knoll, A.H., Saltzman, M.R., 2011a. Geochemical evidence for widespread euxinia in the Later Cambrian ocean. Nature 469, 80–83.

Gill, B.C., Lyons, T.W., Jenkyns, H.C., 2011b. A global perturbation to the sulfur cycle during the Toarcian Ocean Anoxic Event. Earth Planet. Sci. Lett. 312, 484–496.

Goudemand, N., 2014. Time calibrated Early Triassic $\delta^{13}C_{carb}$, $\delta^{18}O_{apatite}$ and SST curves from South China: an update. Albertiana 42, 41–48.

Grasby, S.E., Beauchamp, B., Embry, A., Sanei, H., 2013. Recurrent Early Triassic ocean anoxia. Geology 41, 175–178.

Grice, K., Cao, C., Love, G.D., Böttcher, M.E., Twitchett, R.J., Grosjean, E., Summons, R.E., Turgeon, S.C., Dunning, W., Jin, Y., 2005. Photic zone euxinia during the Permian-Triassic superanoxic event. Science 307 (5710), 706–709.

Grosjean, A.S., Vennin, E., Olivier, N., Caravaca, G., Thomazo, C., Fara, E., Escarguel, G., Bylund, K.G., Jenks, J.F., Stephen, D.A., Brayard, A., 2018. Early Triassic environmental dynamics and microbial development during the Smithian–Spathian transition (Lower Weber Canyon, Utah, USA). Sed. Geol. 363, 136–151.

Habicht, K.S., Canfield, D.E., 1997. Sulfur isotope fractionation during bacterial sulfate reduction in organic-rich sediments. Geochim. Cosmochim. Acta 61, 5351–5361.

Hermann, E., Hochuli, P.A., Bucher, H., Brühwiler, T., Hautmann, M., Ware, D., Roohi, G., 2011. Terrestrial ecosystems on North Gondwana following the end-Permian mass extinction. Gondwana Res. 20, 630–637.

Hermann, E., Hochuli, P.A., Bucher, H., Brühwiler, T., Hautmann, M., Ware, D., Weissert, H., Roohi, G., Yaseen, A., 2012. Climatic oscillations at the onset of the Mesozoic

inferred from palynological records from the North Indian Margin. J. Geol. Soc. Lond. 169, 227–237.
Holser, W.T., Schönlaub, H.P., Attrep, M., Boeckelmann, K., Klein, P., Magaritz, M., Orth, C.J., Fenninger, A., Jenny, C., Kralik, M., 1989. A unique geochemical record at the Permian/Triassic boundary. Nature 337, 39–44.
Horacek, M., Richoz, S., Brandner, R., Krystyn, L., Spötl, C., 2007. Evidence for recurrent changes in Lower Triassic oceanic circulation of the Tethys: The $\delta^{13}C$ record from marine sections in Iran. Palaeogeogr. Palaeoclimatol. Palaeoecol. 252, 355–369.
Horacek, M., Koike, T., Richoz, S., 2009. Lower Triassic $\delta^{13}C$ isotope curve from shallow-marine carbonates in Japan, Panthalassa realm: Confirmation of the Tethys $\delta^{13}C$ curve. J. Asian Earth Sci. 36, 481–490.
Huang, Y., Chen, Z.Q., Wignall, P.B., Zhao, L., 2017. Latest Permian to Middle Triassic redox condition variations in ramp settings, South China: Pyrite framboid evidence. Geol. Soc. Am. Bull. 129, 229–243.
Isozaki, Y., 1997. Permo-Triassic boundary superanoxia and stratified superocean: records from lost deep sea. Science 276, 235–238.
Jattiot, R., Bucher, H., Brayard, A., Monnet, C., Jenks, J.F., Hautmann, M., 2016. Revision of the genus *Anasibirites* Mojsisovics (Ammonoidea): an iconic and cosmopolitan taxon of the late Smithian (Early Triassic) extinction. Pap. Palaeont. 2, 155–188.
Jattiot, R., Brayard, A., Bucher, H., Vennin, E., Caravaca, G., Jenks, J.F., Bylund, K.G., Escarguel, G., 2018. Palaeobiogeographical distribution of Smithian (Early Triassic) ammonoid faunas within the western USA basin and its controlling parameters. Palaeontology 61, 881–904.
Joachimski, M.M., Lai, X.L., Shen, S.Z., Jiang, H.S., Luo, G.M., Chen, B., Chen, J., Sun, Y.D., 2012. Climate warming in the latest Permian and the Permian-Triassic mass extinction. Geology 40, 195–198.
Kampschulte, A., Strauss, H., 2004. The sulfur isotopic evolution of Phanerozoic seawater based on the analysis of structurally substituted sulfate in carbonates. Chem. Geol. 204, 255–286.
Keeling, R.F., Körtzinger, A., Gruber, N., 2010. Ocean deoxygenation in a warming world. Mar. Sci. 2, 199–229.
Komatsu, T., Naruse, H., Shigeta, Y., Takashima, R., Maekawa, T., Dang, H.T., Dinh, T.C., Nguyen, P.D., Nguyen, H.H., Tanaka, G., 2014. Lower Triassic mixed carbonate and siliciclastic setting with Smithian–Spathian anoxic to dysoxic facies, An Chau basin, northeastern Vietnam. Sediment. Geol. 300, 28–48.
Korte, C., Pande, P., Kalia, P., Kozur, H.W., Joachimski, M.M., Oberhänsli, H., 2010. Massive volcanism at the Permian–Triassic boundary and its impact on the isotopic composition of the ocean and atmosphere. J. Asian Earth Sci. 37, 293–311.
Lau, K.V., Maher, K., Altiner, D., Kelley, B.M., Kump, L.R., Lehrmann, D.J., Silva-Tamayo, J.C., Weaver, K.L., Yu, M., Payne, J.L., 2016. Marine anoxia and delayed Earth system recovery after the end-Permian extinction. Proc. Natl. Acad. Sci. (U.S.A.) 113, 2360–2365.
Lehrmann, D.J., Payne, J.L., Felix, S.V., Dillett, P.M., Wang, H., Yu, Y., Wei, J., 2003. Permian–Triassic boundary sections from shallow-marine carbonate platforms of the Nanpanjiang Basin, South China: implications for oceanic conditions associated with the end-Permian extinction and its aftermath. PALAIOS 18 (2), 138–152.
Li, S.Y., Tong, J.N., Liu, K.Y., Wang, F.J., Huo, Y.Y., 2007. The Lower Triassic cyclic deposition in Chaohu, Anhui Province, China. Palaeogeogr. Palaeoclimatol. Palaeoecol. 252, 188–199.
Liang, D., Tong, J.N., Zhao, L.S., 2011. Lower Triassic Smithian-Spathian Boundary at West Pingdingshan Section in Chaohu, Anhui Province. Sci. China D: Earth Sci. 54, 372–379.
Luo, G.M., Kump, L.R., Wang, Y.B., Tong, J.N., Arthur, M.A., Yang, H., Huang, J.H., Yin, H.F., Xie, S.C., 2010. Isotopic evidence for an anomalously low oceanic sulfate concentration following end-Permian mass extinction. Earth Planet. Sci. Lett. 300, 101–111.
Lyons, T.W., Severmann, S., 2006. A critical look at iron paleoredox proxies: New insights from modern euxinic marine basins. Geochim. Cosmochim. Acta 70, 5698–5722.
Marenco, P.J., Corsetti, F.A., Kaufman, A.J., Bottjer, D.J., 2008. Environmental and diagenetic variations in carbonate associated sulfate: an investigation of CAS in the Lower Triassic of the western USA. Geochim. Cosmochim. Acta 72, 1570–1582.
Meyer, K.M., Yu, M., Jost, A.B., Kelley, B.M., Payne, J.L., 2011. $\delta^{13}C$ evidence that high primary productivity delayed recovery from end-Permian mass extinction. Earth Planet. Sci. Lett. 302 (3–4), 378–384.
Meyer, K.M., Yu, M.Y., Lehrmann, D., van de Schootbrugge, B., Payne, J.L., 2013. Constraints on Early Triassic carbon cycle dynamics from paired organic and inorganic carbon isotope records. Earth Planet. Sci. Lett. 361, 429–435.
Nielsen, J.K., Shen, Y., 2004. Evidence for sulfidic deep water during the Late Permian in the East Greenland Basin. Geology 32 (12), 1037–1040.
Orchard, M.J., 2007. Conodont diversity and evolution through the latest Permian and Early Triassic upheavals. Palaeogeogr. Palaeoclimatol. Palaeoecol. 252 (1–2), 93–117.
Ovtcharova, M., Bucher, H., Schaltegger, U., Galfetti, T., Brayard, A., Guex, J., 2006. New Early to Middle Triassic U–Pb ages from South China: calibration with ammonoid biochronozones and implications for the timing of the Triassic biotic recovery. Earth Planet. Sci. Lett. 243 (3–4), 463–475.
Owens, J.D., Gill, B.C., Jenkyns, H.C., Bates, S.M., Severmann, S., Kuypers, M.M.M., Woodfine, R.G., Lyons, T.W., 2013. Sulfur isotopes track the global extent and dynamics of euxinia during Cretaceous Oceanic Anoxic Event 2. Proc. Natl. Acad. Sci. (U.S.A.) 110, 18407–18412.
Payne, J.L., Kump, L.R., 2007. Evidence for recurrent Early Triassic massive volcanism from quantitative interpretation of carbon isotope fluctuations. Earth Planet. Sci. Lett. 256, 264–277.
Payne, J.L., Lehrmann, D.J., Wei, J., Orchard, M.J., Schrag, D.P., Knoll, A.H., 2004. Large perturbations of the carbon cycle during recovery from the end-Permian extinction. Science 305, 506–509.
Piper, D.Z., Link, P.K., 2002. An upwelling model for the Phosphoria sea: A Permian, ocean-margin sea in the northwest United States. AAPG Bull. 86 (7), 1217–1235.
Poulton, S.W., Canfield, D.E., 2005. Development of a sequential extraction procedure for iron: implications for iron partitioning in continentally derived particulates. Chem. Geol. 214, 209–221.
Poulton, S.W., Canfield, D.E., 2011. Ferruginous conditions: a dominant feature of the ocean through Earth's history. Elements 7, 107–112.
Rahm, L., Danielsson, Å., 2007. Spatial heterogeneity of nutrients in the Baltic Proper, Baltic Sea. Estuar. Coast. Shelf Sci. 73 (1–2), 268–278.
Rau, G.H., Riebesell, U., Wolf-Gladrow, D., 1997. CO_{2aq}-dependent photosynthetic ^{13}C fractionation in the ocean: A model versus measurements. Glob. Biogeochem. Cycles 11, 267–278.
Raup, D.M., Sepkoski Jr., J.J., 1982. Mass extinctions in the marine fossil record. Science 215, 1501–1503.
Renne, P.R., Black, M.T., Zhang, Z., Richards, M.A., Basu, A.R., 1995. Synchrony and causal relations between Permian-Triassic boundary crises and Siberian flood volcanism. Science 269, 1413–1416.
Rind, D., 1998. Latitudinal temperature gradients and climate change. J. Geophys. Res. 103, 5943–5971.
Romano, C., Goudemand, N., Vennemann, T.W., Ware, D., Schneebelihermann, E., Hochuli, P.A., Brühwiler, T., Brinkmann, W., Bucher, H., 2013. Climatic and biotic upheavals following the end-Permian mass extinction. Nat. Geosci. 6, 57–60.
Saito, R., Kaiho, K., Oba, M., Takahashi, S., Chen, Z.Q., Tong, J.N., 2013. A terrestrial vegetation turnover in the middle of the Early Triassic. Glob. Planet. Change 105, 152–159.
Schobben, M., Joachimski, M.M., Korn, D., Leda, L., Korte, C., 2014. Palaeotethys seawater temperature rise and an intensified hydrological cycle following the end-Permian mass extinction. Gondwana Res. 26, 675–683.
Sephton, M.A., Looy, C.V., Brinkhuis, H., Wignall, P.B., De Leeuw, J.W., Visscher, H., 2005. Catastrophic soil erosion during the end-Permian biotic crisis. Geology 33 (12), 941–944.
Sepkoski Jr., J.J., 1986. Phanerozoic overview of mass extinction. In: Raup, D.M., Jablonski, D. (Eds.), Patterns and Processes in the History of Life: Report of the Dahlem Workshop on Patterns and Processes in the History of Life, Berlin, 1985, June 16–21. Springer, Berlin, pp. 277–295.
Shen, J., Algeo, T.J., Hu, Q., Zhang, N., Zhou, L., Xia, W., Xie, S., Feng, Q., 2012. Negative C-isotope excursions at the Permian-Triassic boundary linked to volcanism. Geology 40, 963–966.
Shen, J., Schoepfer, S.D., Feng, Q., Zhou, L., Yu, J., Song, H., Wei, H., Algeo, T.J., 2015. Marine productivity changes during the end-Permian crisis and Early Triassic recovery. Earth-Sci. Rev. 149, 136–162.
Shen, J., Feng, Q., Algeo, T.J., Li, C., Planavsky, N.J., Zhou, L., Zhang, M., 2016. Two pulses of oceanic environmental disturbance during the Permian-Triassic boundary crisis. Earth Planet. Sci. Lett. 443, 139–152.
Shen, J., Algeo, T., Planavsky, N.J., Yu, J., Feng, Q., Song, H.J., Song, H.Y., Zhou, L., Chen, J., Rowe, H., 2019. Mercury enrichments provide evidence of Early Triassic volcanism following the end-Permian mass extinction. Earth-Sci. Rev (this volume).
Sobolev, S.V., Sobolev, A.V., Kuzmin, D.V., Krivo-Lutskaya, N.A., Petrunin, A.G., Arndt, N.T., Radko, V.A., Vasiliev, Y.R., 2011. Linking mantle plumes, large igneous provinces and environmental catastrophes. Nature 477, 312–316.
Song, H.J., Wignall, P.B., Chen, Z.Q., Tong, J., Bond, D.P., Lai, X., Zhao, X., Jiang, H., Yan, C., Niu, Z., Chen, J., 2011. Recovery tempo and pattern of marine ecosystems after the end-Permian mass extinction. Geology 39, 739–742.
Song, H.J., Wignall, P.B., Tong, J., Bond, D.P.G., Song, H.Y., Lai, X., Zhang, K.X., Wang, H.M., Chen, Y.L., 2012. Geochemical evidence from bio-apatite for multiple oceanic anoxic events during Permian-Triassic transition and the link with end-Permian extinction and recovery. Earth Planet. Sci. Lett. 353, 12–21.
Song, H.Y., Tong, J.N., Algeo, T.J., Horacek, M., Qiu, H.O., Song, H.J., Tian, L., Chen, Z.Q., 2013a. Large vertical $\delta^{13}C_{DIC}$ gradients in Early Triassic seas of the South China craton: Implications for oceanographic changes related to Siberian Traps volcanism. Glob. Planet. Change 105, 7–20.
Song, H.J., Wignall, P.B., Tong, J., Yin, H., 2013b. Two pulses of extinction during the Permian-Triassic crisis. Nat. Geosci. 6, 52–58.
Song, H.Y., Tong, J.N., Algeo, T.J., Song, H.J., Qiu, H.O., Zhu, Y.Y., Tian, L., Lyons, T.W., Luo, G.M., Kump, L.R., 2014a. Early Triassic seawater sulfate drawdown. Geochim. Cosmochim. Acta 128, 95–113.
Song, H.Y., Tong, J.N., Tian, L., Song, H.J., Qiu, H.O., Zhu, Y.Y., Algeo, T.J., 2014b. Paleo-redox conditions across the Permian-Triassic boundary in shallow carbonate platform of the Nanpanjiang Basin, South China. Sci. China: Earth Sci. 57, 1130–1138.
Song, H.Y., Tong, J.N., Yong, Du, Song, H.J., Tian, L., Chu, D., 2018. Large perturbed marine carbon-nitrogen-sulfur isotopes during Early Triassic. Earth Sci. 43, 3922–3931 (in Chinese with English abstract).
Stanley, S.M., 2016. Estimates of the magnitudes of major marine mass extinctions in earth history. Proc. Natl. Acad. Sci. (U.S.A.) 113, E6325–E6334.
Stebbins, A., Algeo, T.J., Olsen, C., Sano, H., Rowe, H., Hannigan, R., 2018a. Sulfur-isotope evidence for recovery of seawater sulfate concentrations from a PTB minimum by the Smithian-Spathian transition. Earth Sci. Rev (this volume).
Stebbins, A., Algeo, T.J., Krystyn, L., Rowe, H., Brookfield, M., Williams, J., Nye Jr., S.W., Hannigan, R., 2018b. Marine sulfur cycle evidence for upwelling and eutrophic stresses during Early Triassic cooling events. Earth Sci. Rev (this volume).
Sun, Y.D., Joachimski, M.M., Wignall, P.B., Yan, C.B., Chen, Y.L., Jiang, H.S., Wang, L., Lai, X., 2012. Lethally hot temperatures during the Early Triassic greenhouse. Science 338, 366–370.
Sun, Y.D., Wignall, P.B., Joachimski, M.M., Bond, D.P.G., Grasby, S.E., Sun, S., Yan, C.B., Wang, L.N., Chen, Y.L., Lai, X.L., 2015. High amplitude redox changes in the late

Early Triassic of South China and the Smithian–Spathian extinction. Palaeogeogr. Palaeoclimatol. Palaeoecol. 427, 62–78.
Svensen, H., Planke, S., Polozov, A.G., Schmidbauer, N., Corfu, F., Podladchikov, Y.Y., Jamtveit, B., 2009. Siberian gas venting and the end-Permian environmental crisis. Earth Planet. Sci. Lett. 277, 490–500.
Takahashi, S., Oba, M., Kaiho, K., Yamakita, S., Sakata, S., 2009. Panthalassic oceanic anoxia at the end of the Early Triassic: A cause of delay in the recovery of life after the end-Permian mass extinction. Palaeogeogr. Palaeoclimatol. Palaeoecol. 274, 185–195.
Thomazo, C., Vennin, E., Brayard, A., Bour, I., Mathieu, O., Elmeknassi, S., Olivier, N., Escarguel, G., Bylund, K.G., Jenks, J., 2016. A diagenetic control on the Early Triassic Smithian–Spathian carbon isotopic excursions recorded in the marine settings of the Thaynes Group (Utah, USA). Geobiology 14, 220–236.
Thomazo, C., Brayard, A., Elmeknassi, S., Vennin, E., Olivier, N., Caravaca, G., Escarguel, G., Fara, E., Bylund, K.G., Jenks, J.F., Stephen, D.A., Killingsworth, B., Sansjofre, P., Cartigny, P., 2018. Multiple sulfur isotope signals associated with the late Smithian event and the Smithian/Spathian boundary. Earth Sci. Rev (this volume).
Tian, L., Tong, J.N., Algeo, T.J., Song, H.J., Song, H.Y., Chu, D., Shi, L., Bottjer, D.J., 2014. Reconstruction of Early Triassic ocean redox conditions based on framboidal pyrite from the Nanpanjiang Basin, South China. Palaeogeogr. Palaeoclimatol. Palaeoecol. 412, 68–79.
Tong, J.N., Zakharov, Y.D., Orchard, M.J., Yin, H.F., Hansen, H.J., 2004a. Proposal of Chaohu section as the GSSP candidate of the Induan-Olenekian boundary. Albertiana 29, 13–27.
Tong, J.N., Zakharov, Y.D., Wu, S.B., 2004b. Early Triassic ammonoid succession in Chaohu, Anhui Province. Acta Palaeontol. Sin. 43, 192–204.
Tong, J.N., Zuo, J.X., Chen, Z.Q., 2007. Early Triassic carbon isotope excursions from South China: proxies for devastation and restoration of marine ecosystems following the end-Permian mass extinction. Geol. J. 42, 371–389.
Veizer, J., Holser, W.T., Wilgus, C.K., 1980. Correlation of $^{13}C/^{12}C$ and $^{34}S/^{32}S$ secular variations. Geochim. Cosmochim. Acta 44, 579–587.
Walker, J.C., 1986. Global geochemical cycles of carbon, sulfur and oxygen. Mar. Geol. 70 (1–2), 159–174.
Wei, H.Y., Shen, J., Schoepfer, S.D., Krystyn, L., Richoz, S., Algeo, T.J., 2015. Environmental controls on marine ecosystem recovery following mass extinctions, with an example from the Early Triassic. Earth-Sci. Rev. 149, 108–135.
Wignall, P.B., Twitchett, R.J., 1996. Oceanic anoxia and the end Permian mass extinction. Science 271, 1155–1158.
Wignall, P.B., Bond, D.P., Sun, Y., Grasby, S.E., Beauchamp, B., Joachimski, M.M., Blomeier, D.P., 2016. Ultra-shallow-marine anoxia in an Early Triassic shallow-marine clastic ramp (Spitsbergen) and the suppression of benthic radiation. Geol. Mag. 153 (2), 316–331.
Wilkin, R.T., Arthur, M.A., 2001. Variations in pyrite texture, sulfur isotope composition, and iron systematics in the Black Sea; evidence for late Pleistocene to Holocene excursions of the O_2-H_2S redox transition. Geochim. Cosmochim. Acta 65, 1399–1416.
Wilkin, R.T., Barnes, H.L., Brantley, S.L., 1996. The size distribution of framboidal pyrite in modern sediments: An indicator of redox conditions. Geochim. Cosmochim. Acta 60, 3897–3898.
Winguth, C., Winguth, A.M., 2012. Simulating Permian–Triassic oceanic anoxia distribution: implications for species extinction and recovery. Geology 40 (2), 127–130.
Yan, D., Chen, D., Wang, Q., Wang, J., Wang, Z., 2009. Carbon and sulfur isotopic anomalies across the Ordovician–Silurian boundary on the Yangtze Platform, South China. Palaeogeogr. Palaeoclimatol. Palaeoecol. 274 (1–2), 32–39.
Yin, H.F., Huang, S.J., Zhang, K.X., Hansen, H.J., Yang, F.Q., Ding, M.H., Bei, X.M., Sweet, W.C., 1992. The effects of volcanism on the Permo-Triassic mass extinction in South China. In: Yang, Z., Dickins, J.M., Yin, H. (Eds.), Permo-Triassic Events in the Eastern Tethys. Cambridge University Press, pp. 146–157.
Zhang, L., Zhao, L., Chen, Z.Q., Algeo, T.J., Chen, J., Wang, R., Chen, L., Hou, J., Yang, L., Qiu, H., Feng, X., Wang, X., 2015. Amelioration of marine environments at the Smithian-Spathian boundary, Early Triassic. Biogeosciences 12, 1597–1613.
Zhang, F., Algeo, T.J., Romaniello, S.J., Cui, Y., Zhao, L., Chen, Z.Q., Anbar, A.D., 2018a. Congruent Permian-Triassic $\delta^{238}U$ records at Panthalassic and Tethyan sites: Confirmation of global-oceanic anoxia and validation of the U-isotope paleoredox proxy. Geology 46 (4), 327–330.
Zhang, F., Romaniello, S.J., Algeo, T.J., Lau, K.V., Clapham, M.E., Richoz, S., Herrmann, A.D., Smith, H., Horacek, M., Anbar, A.D., 2018b. Multiple episodes of extensive marine anoxia linked to global warming and continental weathering following the latest Permian mass extinction. Sci. Adv. 4 (4), e1602921.
Zhang, L., Orchard, M.J., Brayard, A., Algeo, T.J., Zhao, L.S., Chen, Z.Q., 2019. The Smithian/Spathian boundary (late Early Triassic): a review of ammonoid, conodont, and carbon-isotopic criteria. Earth-Sci. Rev (this volume).
Zhao, L.S., Orchard, M.J., Tong, J.N., Sun, Z.M., Zuo, J.X., Zhang, S.X., Yun, A.L., 2007. Lower Triassic conodont sequence in Chaohu, Anhui Province, China and its global correlation. Palaeogeogr. Palaeoclimatol. Palaeoecol. 252, 24–38.